



UPPSALA
UNIVERSITET

*Digital Comprehensive Summaries of Uppsala Dissertations
from the Faculty of Science and Technology 682*

Design of carbide-based nanocomposite coatings

ERIK LEWIN



ACTA
UNIVERSITATIS
UPSALIENSIS
UPPSALA
2009

ISSN 1651-6214
ISBN 978-91-554-7636-6
urn:nbn:se:uu:diva-109427

Dissertation presented at Uppsala University to be publicly examined in Högssalen, Ångströmlaboratoriet, Lägerhyddsvägen 1, Uppsala, Friday, November 27, 2009 at 10:15 for the degree of Doctor of Philosophy. The examination will be conducted in English.

Abstract

Lewin, E. 2009. Design of carbide-based nanocomposite coatings. Acta Universitatis Upsaliensis. *Digital Comprehensive Summaries of Uppsala Dissertations from the Faculty of Science and Technology* 682. 83 pp. Uppsala. ISBN 978-91-554-7636-6.

In this thesis research on synthesis, microstructure and properties of carbide-based coatings is reported. These coatings are electrically conducting, and can be tailored for high hardness, low friction and wear, along with load-adaptive behaviour. Tailoring these properties is achieved by controlling the relative phase content of the material. Coatings have been synthesised by dc magnetron sputtering, and their structures have been characterised, mainly by X-ray photoelectron spectroscopy and X-ray diffraction.

It has been shown that nanocomposites comprising of a nanocrystalline transition metal carbide (nc-MeC_x , $\text{Me} = \text{Ti, Nb or V}$) and an amorphous carbon (a-C) matrix can result in low contact resistance in electrical contacts. Such materials also exhibit low friction and high resistance to wear, making them especially suitable for application in sliding contacts. The lowest contact resistance is attained for small amounts of the amorphous carbon phase.

It has been shown that specific bonding structures are present in the interface between nc-TiC_x and the a-C phases in the nanocomposite. It was found in particular that Ti3d and C2p states are involved, and that considerable charge transfer occurs across the interface, thereby influencing the structure of the carbide.

Further design possibilities were demonstrated for TiC_x -based nanocomposites by alloying them with weakly carbide-forming metals, *i.e.*, $\text{Me} = \text{Ni, Cu or Pt}$. Metastable supersaturated solid solution carbides, $(\text{Ti}_{1-x}\text{Me}_x)\text{C}_y$, were identified to result from this alloying process. The destabilisation of the TiC_x -phase leads to changes in the phase distribution in the deposited nanocomposites, thus providing further control over the amount of carbon phase formed. Additional design possibilities became available through the decomposition of the metastable $(\text{Ti}_{1-x}\text{Me}_x)\text{C}_y$ phase through an appropriate choice of annealing conditions, yielding either more carbon phase or a new metallic phase involving Me . This alloying concept was also studied theoretically for all 3d transition metals using DFT techniques.

It has also been demonstrated that Ar-ion etching (commonly used in the analysis of carbide based nanocomposites) can seriously influence the result of the analysis, especially for materials containing metastable phases. This implies that more sophisticated methods, or considerable care are needed in making these analyses, and that many of the earlier published results could well be in error.

Keywords: chemistry, thin film, dc magnetron sputtering, carbide, nanocomposite, PVD, solid solution

Erik Lewin, Department of Materials Chemistry, Inorganic Chemistry, Box 538, Uppsala University, SE-75121 Uppsala, Sweden

© Erik Lewin 2009

ISSN 1651-6214

ISBN 978-91-554-7636-6

urn:nbn:se:uu:diva-109427 (<http://urn.kb.se/resolve?urn=urn:nbn:se:uu:diva-109427>)

Papers included in the thesis

This thesis is based on the following papers, which are referred to in the text by their Roman numerals.

- I **Influence of sputter damage on the XPS analysis of metastable nanocomposite coatings**
E. Lewin, M. Gorgoi, F. Schäfers, S. Svensson, U. Jansson
Surface and Coatings Technology **204**, 455-462 (2009)
- II **On the origin of a third spectral component of C1s XPS-spectra for nc-TiC/a-C nanocomposite thin films**
E. Lewin, P. O. Å. Persson, M. Lattemann, M. Stüber, M. Gorgoi, A. Sandell, C. Ziebert, F. Schäfers, W. Braun, J. Halbritter, S. Ulrich, W. Eberhardt, L. Hultman, H. Siegbahn, S. Svensson, U. Jansson
Surface and Coatings Technology **202**, 3563-3570 (2008)
- III **Electronic structure and chemical bonding of nc-TiC/a-C nanocomposites**
M. Magnusson, E. Lewin, L. Hultman, U. Jansson
Physical Review B, submitted (September 2009)
- IV **Nanocomposite nc-TiC/a-C thin films for electrical contact applications**
E. Lewin, O. Wilhelmsson and U. Jansson
Journal of Applied Physics **100**, 054303 (2006)
- V **Industrialisation Study of Nanocomposite nc-TiC/a-C Coatings for Electrical Contact Applications**
E. Lewin, E. Olsson, B. André, T. Joelsson, Å. Öberg, U. Wiklund, H. Ljungcrantz, U. Jansson
Plasma Processes and Polymers, published online (2009)
DOI: 10.1002/ppap.200932303

- VI **Selective alloying of transition metal carbides**
M. Rålander, E. Lewin, O. Wilhelmsson, B. Sanyal,
M. Klintenberg, O. Eriksson, U. Jansson
in manuscript (October 2009)
- VII **Sputtered Ti-Ni-C thin films for tribological
and electrical contact applications**
E. Lewin, B. André, S. Urbonaite, U. Wiklund, U. Jansson
Journal of Applied Physics, submitted (September 2009)
- VIII **Friction and contact resistance of nanocomposite
Ti-Ni-C coatings**
B. André, E. Lewin, U. Jansson, U. Wiklund
In manuscript (October 2009)
- IX **Carbide and nanocomposite thin films in the Ti-Pt-C system**
E. Lewin, S. Buchholt, J. Lu, L. Hultman, A. Lloyd Spetz,
U. Jansson
Thin solid films, submitted (October 2009)

Reprints were made with permission from the respective publishers.

My contributions

In papers where I am the first author I have clearly been responsible for the scientific discussion and also at least a major part of the experimental work. Specifically the following can be noted:

Publication I: I have planned and executed all the experimental work, and written the manuscript.

Publication II: I have been responsible for planning the study and writing the manuscript, have also synthesised half of samples used in study and performed the majority of the characterisation, although none of the TEM.

Publication III: For this work I have synthesised samples and performed XRD and XPS analysis. I have also been an active partner in the scientific discussion and written parts of the manuscript.

Publication IV: I have been responsible for planning, experimental work and writing of the manuscript.

Publication V: I have characterised the samples with regards to microstructure and properties, as well as written the manuscript

Publication VI: For this paper I have provided supporting experimental data in the form of XPS and XRD data from samples synthesised in other studies. Have also written small parts of the manuscript and been active in the scientific discussion.

Publication VI: I have been responsible for planning the study, synthesised the materials and characterised their microstructure, as well as written the majority of the manuscript

Publication VIII: For this study I have synthesised the samples and performed some of the characterisation and have contributed to the writing of the manuscript and the scientific discussion.

Publication IX: I have synthesised about half of the samples, performed XRD- and XPS-characterisation, and have done most of the writing.

In the thesis some results are included, that neither are published nor in manuscript. In particular these results deal with coatings in the Ti-Cu-C system which I have synthesised and characterised; with interfacial bonding in nc-TiC_x/a-C nanocomposites for which new theoretical simulations were performed after suggestions by me; and with the possible growth of graphene on epitaxial carbides, for which I have provided the carbide coatings and performed some characterisation.

Other publications to which the author has contributed

Deposition and characterization of ternary thin films within the Ti-Al-C system by DC magnetron sputtering

O. Wilhelmsson, J.P. Palmquist, E. Lewin, J. Emmerlich, P. Eklund, P.O. Å. Persson, H. Högberg, S. Li, R. Ahuja, O. Eriksson, L. Hultman, U. Jansson
Journal of Crystal Growth, 291 (2006), 290-300

HIKE experiments at KMC-1: Recent Analysis of Thin Film Nanocomposites

E. Lewin, E. Johansson, A. Sandell, M. Gorgoi, F. Schäfers, W. Braun, H. Siegbahn, M. Stüber, U. Jansson, S. Svensson, W. Eberhardt
BESSY Annual Report 2006, 503-504

Kontaktelement och kontakthanordning

E. Lewin, O. Wilhelmsson and U. Jansson, filed by ABB Research Ltd. and Impact Coatings AB
Swedish patent nr. SE 0501667-0, publication nr. SE 528 908 granted March 13th 2007.

Design of nanocomposite low-friction coatings

O. Wilhelmsson, M. Rålander, M. Carlsson, E. Lewin, B. Sanyal, U. Wiklund, O. Eriksson, U. Jansson
Advanced Functional Materials, 17 (2007), 1611-1616

Conductive nanocomposite ceramics as tribological and electrical contact materials

Å. Öberg, Å. Kassman, B. André, U. Wiklund, M. Lindquist, E. Lewin, U. Jansson, H. Högberg, T. Joelsson, H. Ljungcrantz
The European Physical Journal - Applied Physics, accepted April 2009

Growth and structure properties of Mg:C thin films prepared by dc magnetron discharge

A.S. Ingason, A.K. Eriksson, E. Lewin, J. Jensen, S. Olafsson
Thin solid films, accepted October 2009

A novel wear-resistant magnetic thin film material based on a $\text{Ti}_{1-x}\text{Fe}_x\text{C}_{1-y}$ nanocomposite alloy

S. Bijelovic, M. Rålander, O. Wilhelmsson, E. Lewin, B. Sanyal, U. Jansson, O. Eriksson, P. Svedlindh
submitted to Physical review B, July 2009

Contents

1. Introduction	9
2. Carbide-based materials	14
Binary carbide-based nanocomposites	16
Ternary systems	19
3. Electrical contact resistance	22
4. Methods	24
Magnetron sputtering	24
Microstructural and chemical characterisation	27
X-ray photoelectron spectroscopy (XPS)	27
X-ray diffraction (XRD)	31
Other analysis techniques	33
Assessment of properties	34
Theoretical modelling	35
5. Results	37
Binary Me-C materials	37
Carbides and nanocomposites in the Ti-C system	37
Up-scaling / industrialisation of Ti-C coatings	46
Nanocomposites in the V-C, Zr-C and Nb-C systems	48
Alloying Ti-C: ternary Ti-Me-C materials	49
Theoretical results	50
Ti-Ni-C materials	51
Ti-Pt-C materials	56
Ti-Cu-C materials	59
Properties of carbide and nanocomposite coatings	61
Template based graphene synthesis on epitaxial carbide	67
6. Concluding remarks	70
7. Acknowledgements	72
8. References	74
9. Sammanfattning på svenska	80

Abbreviations

a-	prefix for an amorphous phase
a.u.	arbitrary units
at.%	Atomic percent
DFT	Density functional theory
DOS	Density of states
E_b	electron binding energy
ERDA	Elastic recoil detection analysis
ESCA	Electron spectroscopy for chemical analysis
fcc	face centred cubic (crystal structure)
HAXPES	Hard X-ray photoelectron spectroscopy
HIKE	High kinetic energy
HRTEM	High resolution transmission electron microscopy
LEED	Low energy electron diffraction
nc-	prefix for a nanocrystalline phase
PES	Photoelectron spectroscopy
PVD	Physical vapour deposition
SEM	Scanning electron microscopy
STEM	Scanning transmission electron microscopy
SXA	Soft X-ray absorption
SXE	Soft X-ray emission
TEM	Transmission electron microscopy
XAS	X-ray absorption spectroscopy
XES	X-ray emission spectroscopy
XPS	X-ray Photoelectron Spectroscopy
XRD	X-ray diffraction
XRR	X-ray reflectivity
Å	Ångström = 10^{-10} meter

1. Introduction

The development of materials has always been a driving force in human advancement. This is amply indicated by the fact that the early stages of civilisation commonly are referred to with their dominant tool material: i.e. the stone, bronze and iron ages. Without the progress of materials science, many scientific or technological developments would never have been possible. As technology and science have advanced the number and diversity of materials available for tools, construction and other applications have increased continuously. The idea of using different materials for different applications, depending on their properties, is hardly new, but the technological and scientific advances of the 20th century has brought the idea to new levels. To choose or synthesise new materials based on knowledge on how their structure on an atomic level will provide sought after properties is still an emerging craft.

The field of materials science is a truly interdisciplinary field, requiring knowledge from the traditional academic sciences of chemistry and physics, as well as from engineering. This is symptomatic of a field where fundamental and applied science meet. Evaluating mechanical, optical and electrical properties such as hardness, transparency and resistivity are part of applied science. But to move beyond the realm of trial-and-error and into science, a more fundamental understanding of the origin of these properties is required. Understanding the chemical bonding between elements, how elements form different phases and how to synthesise new compounds is traditionally the realm of chemistry. To be able to determine and analyse the structure of a material, one must turn to spectroscopic and microscopic techniques which together with properties such as electronic transport traditionally are in realm of physics. Testing the properties of new materials, and transferring the synthesis from the laboratory to industrial reality is in the realm of engineering.

There is no single theoretical model that simply can predict the properties of a hypothetical or modified known material. For this reason materials design is presently exploring many different, partly interconnected minor areas where models can be built up to explain variations in properties and hence be used to design a specific combinations of properties suited for certain application.

One way to attain a combination of properties that pure compounds do not possess is to combine more than one compound in one material. A very common and conceptually simple way to do this is to provide a different surface – a coating. Since any chemical or mechanical contact first will occur at the surface, a coating may have a very large impact on the total performance of a component. A very simple example of this is paint; which provides a ‘pretty’ look and protection towards a potentially harsh environment. This is especially suited for a material which doesn’t have a ‘pretty’ finish or resistance to the environment, but instead provides a structural strength. This concept of coatings on the surface which alters the total properties of a component has during the 20th century expanded into an entire industrial sector, working with many types of coating materials. These are sometimes applied in a way similar to paint, but more often synthesised (“grown”) on the component during a so called deposition process. The variety of different methods to deposit coating materials are almost as vast as the ever expanding choice of materials, ranging from polymers (e.g. low-stick coatings on frying pans) through ceramics (e.g. anti-scratch coatings on plastics) to metals (heat-reflective coatings on architectural glass). But coatings are not only used to modify the surface of a component, they can also be used to build up a component, for example coatings are included in the production of electronics, where layers of conductive and insulating materials are patterned and combined to form integrated circuits.

Another way to attain combinations of properties from several different compounds is to form a composite, i.e. a mixed material consisting of several different materials. An easily understood, and old, example is reinforced concrete where iron bars are used to reinforce the concrete, resulting in a material which is more crack-resistant than pure concrete and withstands higher pressures than pure iron. But the composite is less crack-resistant than pure iron and does not withstand as high pressures as pure concrete. As a first approximation the properties of composites can be estimated by the rule of mixing, a weighted average of the constituents.

If one of the phases in the composite has one, two or three dimensions of less than 100 nanometres (10^{-9} m), the composite is called a *nanocomposite*. For the same reasons that nanotechnology in general has received a lot of attention from the 1980’s and onward, this type of composite is particularly interesting. There are mainly two phenomena that make materials of nanometre sizes special from scientific point-of-view. The dimensions in question are in the same order of magnitude as critical lengths in physical phenomena (e.g. the mean free path of electrons and phonons) and chemical bonds (typically $1 \cdot 10^{-10}$ to $3 \cdot 10^{-10}$ m). In the nanometre-range one may thus find modified optical, electrical and mechanical properties. Additionally if the struc-

tures of the material are needle-like or flat, the reduced dimensions may lead to that the material can be considered one- or two-dimensional. For some physical phenomena this can introduce further peculiar properties in e.g. electrical conduction. Secondly, the relative amount of interfaces increases inversely proportional to the length scale. This means that, when length scale reaches nanometres the interfaces make out an appreciable portion of the total material. Since the interface by definition represents a distortion of the structure of a material, and usually contain different chemical bonding, different macroscopic (e.g. optical, electrical or mechanical) properties can be expected when the volume of the interfaces get into the same order of magnitude as the bulk of the material. Hence, for nanocomposites the traditional mixing rules described above for the example of reinforced concrete do not apply. Other types of combined or new properties may be attainable. Nanocomposite materials have actually been used for many centuries, but without a scientific understanding, which still is emerging.



Figure 1.1 A historical example of nanotechnology from Roman times: the Lycurgus cup, in reflective (left) and transmitted (right) light.
© Trustees of the British Museum.

One interesting historic example of nanocomposites is the use gold (or silver) particles in the range of a few tens of nanometers, which dependent of size can show different colours; and if contained in glass, the glass may also exhibit different colours in reflection and transmission. Such materials have been known from Roman times, and are mentioned in the 4th century work *Historiae Augustae* where a gift is mentioned in a quoted letter*

* It should be noted that this letter which supposedly is from Emperor Hadrian Augustus to his brother-in-law Servianus most likely is a falsification, as much of the *Historiae Augusta*. But the fact remains that a 4th century author writes about cups with spectacular optical features, worthy gifts from an Emperor.

“I am sending you over some cups, changing colour and variegated, presented to me by the priest of a temple and now dedicated particularly to you and my sister. I should like you to use them at banquets on feast-days.”¹

The fact that such glass work existed in Roman times is proved by a few remaining objects. The most famous of which is probably the Lycurgus cup from the 4th century AD, now at the British museum, London. This cup is green in reflective light, and bright red in transmitted light, see Figure 1.1. The craftsmanship to produce this type of material evidently existed in 4th century AD, but was then lost.² The art of producing a similar colorant was rediscovered during the 17th century and known under the name “Purple of Cassius”.³ Over the years this colorant intrigued lay people as well as scientists, including Swedish chemist Jöns Jacob Berzelius, who attempted to determine the stoichiometry of this assumed compound.^{4, 5} The idea that the observed colours could be an effect of small particles was first suggested by Faraday in 1857.⁶ A model based on classical physics was presented by Mie in 1908,⁷ and a comprehensive theoretical model was published as late as 2003.⁸

It is only during the last two to three decades analytical tools have become available, that enable scientists to properly analyse materials of nanometre dimensions to such an extent that their structure (at least to a high degree) can be determined, and properties explained. Hence the field of nanocomposites is still greatly unexplored and a very active field for research.

A field which can benefit from development of new materials is the field of electrical contact coatings. Electrical contacts are an important part of our electrified society. They exist all around us in our vehicles, hand-held and stationary electronics, and are also plentiful in the electricity distribution system. A malfunctioning electrical contact is at best an inconvenience, in worst case cause of a disaster. An example of the latter is the events causing the large blackout in September 2003, when parts of southern Sweden (anything south of the line Varberg - Norrköping) as well as Sjælland and Bornholm in Denmark lost all electricity. The primary cause of the blackout was a malfunctioning disconnector at a high voltage switchgear. A load and current-bearing, rotating joint in the disconnector failed due to heating which caused a structural collapse of the component. The heating was caused by poor electrical contact in the joint. Due to unlucky circumstances this collapse caused an electrical arc, short-circuiting two 400 kV phases. The blackout effected about 857 000 customers in Sweden and lasted up to five hours; the cost to Swedish society was estimated to 500 million SEK.⁹

Traditionally electrical contact members consist of a bulk material which is cheap and highly electrically conductive (e.g. copper, brass or aluminium) with a coating of reasonably noble and soft metal (e.g. gold or silver). This

coating provides ‘good’ electrical contact properties by giving protection against corrosion and low electrical resistance. There are two main drawbacks of these noble metal coatings: noble metals are expensive, and the softness which gives a low constriction resistance can also cause the coatings to smear upon repeated or continuous sliding which is the case for a contact member which is often dis- and reconnected, or used in rotational connection. This smearing will cause a high friction and wear, which will severely reduce the lifetime of the contact component. There is hence a need for new materials that provide a combination of ‘good’ electrical contact properties and low friction and wear.

The nanocomposite coatings materials studied in this thesis represent an alternative to traditional electrical contact materials. The nanocomposites consist of hard, electrically conductive particles in the range of a few to tens of nanometer in diameter, embedded in a softer, less conductive matrix phase. This type of composite gives several inherent design possibilities. The choice of particle and matrix phases need not be discrete choices, but can be fine-tuned by chemical modifications. Also the relative amounts of phases and their dimensions give further design possibilities. In particular this thesis deals with nanocomposites based on transition metals carbides (particle phase) and amorphous carbon (matrix phase).

The research leading to the present thesis has been conducted in an environment of collaboration between academia and industry. This means that the aims of the research have been two-fold: fundamental research and development of potentially useful materials. The choice of properties to study has hence been an effect of the interests of the industrial partners. Here this has lead to a focus on the electrical and tribological properties of coatings suitable for electrical contacts. The aim of the fundamental research has been to increase the understanding of carbide-based nanocomposites, what controls their properties and how these can be modified by changes in material chemistry or morphology.

2. Carbide-based materials

Carbides are compounds of carbon and metals or B and Si. Metallic carbides are formed between C and transition metals, and are sometimes called interstitial carbides because C occupies interstitial sites in the structure. The research in the present thesis is limited to this type of carbides, which generally are hard, electrically conductive, refractory, and have thus found technical applications, in e.g. cutting tools.¹⁰⁻¹²

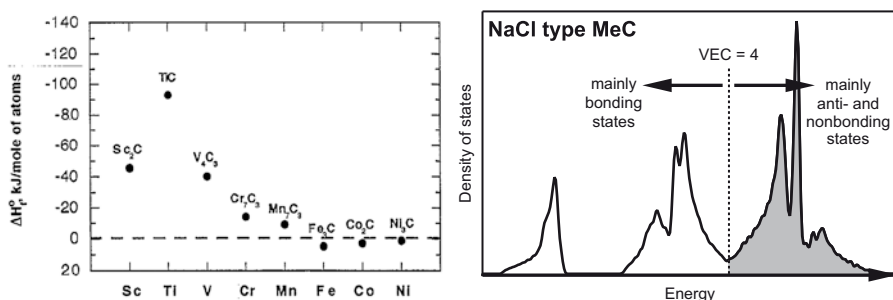


Figure 2.1 Left, experimental formation enthalpies for a number of transition metal carbides. Reprinted from with permission of Elsevier from Meschel and Kleppa.¹³ Right, a typical density of states for transition metal carbides with NaCl type structure.

The transition metal carbides have varying stability in the periodic table. This is exemplified by the formation enthalpy for some 3d transition metal carbides in Figure 2.1 (left), and shown schematically in Figure 2.2. Early transition metals (groups 3 through 6) are strong carbide forming metals and form thermodynamically stable carbide phases. Late transition metals in group 8 through 10 are weak carbide formers and only metastable carbides, such as Fe₃C (cementite), Ni₃C and PtC exist.¹²⁻¹⁴ The coin metals in group 11 do not form any carbide phases, nor does the elements in group 12.¹¹

The maximum carbide stability is reached in group 4; stability thereafter decreases with the group number, see Figure 2.1 (left). The reason for this is in the bonding, and can be understood from band filling.^{12, 15-17} The right part of the Figure 2.1 shows a typical density of states (DOS) for transition metal carbides with NaCl type structure. Bonding states are found below the centre of the region of low DOS. Higher energy states are anti- or nonbonding. For a valence electron concentration of 4 (which group 4 mono carbides

	1																18
1	H	2															He
2	Li	Be															
3	Na	Mg	3	4	5	6	7	8	9	10	11	12	13	14	15	16	17
4	K	Ca	Sc	Ti	V	Cr	Mn	Fe	Co	Ni	Cu	Zn	Al	Si	P	S	Cl
5	Rb	Sr	Y	Zr	Nb	Mo	Tc	Ru	Rh	Pd	Ag	Cd	Ga	Ge	As	Se	Br
6	Cs	Ba	La	Hf	Ta	W	Re	Os	Ir	Pt	Au	Hg	Tl	Pb	Bi	Po	At
																	Rn

Figure 2.2 The periodic table, with the carbide binding abilities of transition metals indicated by shading. Dark grey signifies that thermodynamically stable carbides are known; and light grey signifies that only metastable carbides are known.

have), the Fermi level will be in the middle of the pseudo gap, hence filling all bonding and a minimum of antibonding states. The carbide stability consequently decreases if valence electron concentration deviates from 4; and the group 4 elements (Ti, Zr and Hf) form the most stable carbides. They all have the cubic NaCl type structure, which is shown in Figure 2.3 (top, left). The filling of anti-bonding states also leads to structural changes. Group 5 and 6 transition metals also form other carbides, based on either octahedral or trigonal prismatic structural elements.¹² The bonding in transition metal carbides has covalent, ionic and metallic contributions. The metallic and covalent bonding can be understood from overlap of atomic orbitals.¹² This is shown schematically in Figure 2.3. C 2p-Me d (π and σ) overlap give the covalent bonding, see Figure 2.3 (bottom), while Me d-d σ overlap give the metallic bonding, see Figure 2.3 (top, right). The ionic contribution comes from a charge-transfer from the metal to the more electronegative carbon.

Generally the transition metal carbides, and are found to have extensive homogeneity ranges and are hence written MeC_x, see binary phase diagrams in Figure 2.4.¹² The substoichiometric carbides have varying degree of carbon vacancies, something which generally affect their properties. The electrical conductivity of the transition metal carbides is lower than corresponding metals. The resistivity is usually in the order of 40-200 $\mu\Omega\text{cm}$, decreasing with (and mainly dependent of) the carbon-content of the carbide. The resistivity is found to increase with temperature, which shows the metallic conduction mechanism.^{12, 18} The mechanical properties of the TiC_x (and presumably the other transition metal carbides as well) also depend on the stoichiometry. For example, the Young's modulus and hardness for TiC_x has been found to vary, between 200-460 GPa and 15-28 GPa, respectively, within the homogeneity range.¹²

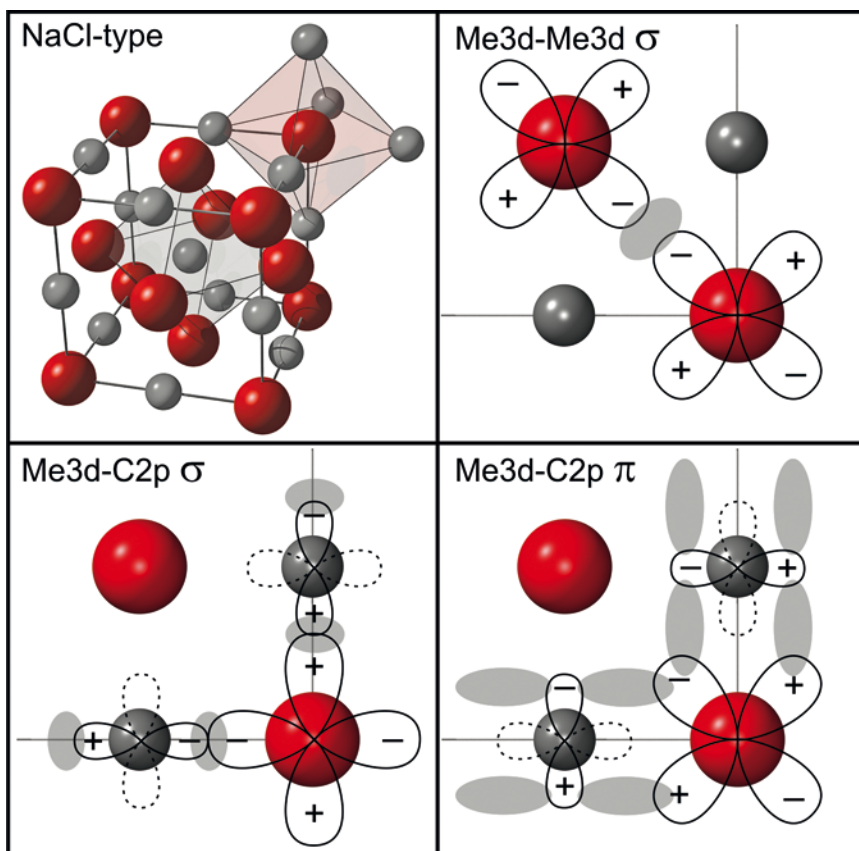


Figure 2.3 Top, left shows the NaCl type crystal structure adapted by the carbides studied in the present thesis. The octahedral surrounding of both species shown by polyhedra. Right and bottom, the covalent and metallic bonding in the (100)-plane. Me and C atoms are represented by red and grey spheres, respectively. Grey areas are guides for the eye, to visualise the bonding.

Binary carbide-based nanocomposites

As can be understood from the above description of carbide phases, the binary phase diagrams of early transition metals and carbon hence typically consist of: Me, one or several carbide phases, and graphite, as well as two-phase regions where composites are expected, see Figure 2.4 where systems relevant for this thesis are shown. When composites are synthesised using methods such as sputter deposition, which operates far from thermodynamical equilibrium, some deviations from equilibrium can be expected: instead of graphite, an amorphous carbon (a-C) phase is commonly formed. The structure of this phase is strongly influenced by the deposition technique

and parameters. From non-reactive sputtering a mainly sp^2 -bonded a-C phase is obtained.¹⁹ The obtained carbide phase is usually nanocrystalline. In coatings deposited by sputtering, the two-phase region above ~50 at.% C is hence expected to consist of the nc-MeC_x/a-C nanocomposite.

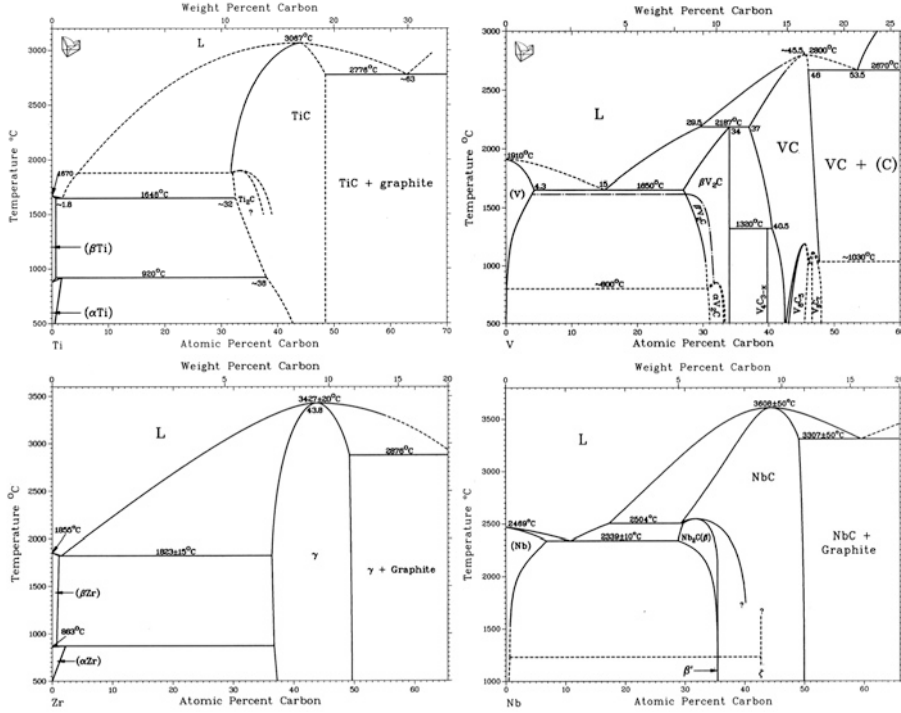


Figure 2.4 Binary phase diagrams of Ti-C, V-C, Zr-C and Nb-C systems, reproduced from Massalski.²⁰

The nc-MeC_x/a-C nanocomposites have been extensively studied the past decades with a large focus on applicable properties such as high hardness or low friction. The intriguing feature, both for applied and fundamental research, of nc-Me_x/a-C nanocomposites is the inherent design possibilities: Changes of the relative amount of phases and / or grain sizes, as well as choice of Me give many possibilities to influence material properties. Much of the academic interest has been on the nc-TiC_x/a-C system,²¹⁻²⁹ but also other systems have been studied.²⁹⁻³¹

Both mechanical and tribological properties of nc-TiC_x/a-C nanocomposites have been found to be controlled by the amount of a-C matrix and the grain sizes. Depending on the relative amount of matrix phase friction, coefficients between 0.5 and 0.1 have been observed, with the lowest wear and friction generally obtained for coatings with a rather large amount of matrix phase (acting as solid lubricant).²⁵ The hardness on the other hand is dependent on the combination of grain size and amount of matrix phase, and

for the nanocomposite values between 5 and 35 GPa have been reported.²⁵ Highest hardness has been obtained for coatings with a very thin matrix (tissue) phase between TiC_x crystallites small enough to be dislocation free.^{25, 32} The combination of a (comparably) soft a-C matrix and hard nc-TiC crystallites also allows for the design of hard, load-adaptive coatings that can be subjected to high loading without brittle failure.²¹

The electrical conduction of the nc- $\text{MeC}_x/\text{a-C}$ nanocomposites is the result of the combination of the metallically conductive MeC_x phase and the poorly conductive a-C phase. Generally it is found that the conductivity is strongly dependent on the total amount of carbon, and varies from $10^1 \mu\Omega\text{cm}$ to $10^{14} \mu\Omega\text{cm}$.^{26, 33, 34} There are indications that the conduction mechanism is highly dependent on the microstructure of the coating, and mechanisms have been proposed,^{35, 36} but no complete understanding exist.

Since the relative amount of phases is an important design tool in these systems, it should be noted that the non-equilibrium synthesis conditions also here can lead to deviations from phase diagrams. The two-phase regions may both grow and shrink compared to phase diagrams.³⁷ Limited diffusion at the growing surface leads to an increase solubility of Me in the a-C phase; up to a couple of atomic % has been observed.²² Also the carbide stoichiometry can be affected of the growth kinetics. Substoichiometric carbide phase can be formed, despite the presence of an a-C phase. This behaviour is not rule, but can be observed in works by several research groups.²⁶⁻²⁸

Despite the intensive research there is still room for fundamental research. One aspect not yet understood is the interface between the carbon and carbide, which is an important factor in understanding the properties of nc- $\text{TiC}_x/\text{a-C}$ nanocomposites.³⁸ It has been suggested that an unidentified spectral feature of C1s XPS spectra (in the present work denoted C-Ti*) is connected with a special bonding at this interface.^{23, 29, 39, 40} But other explanations for the spectral observation has also been suggested, such as a (possibly by ion bombardment) distorted TiC-phase,^{23, 26, 39-42} separate Ti_xC_y clusters / phases,^{43, 44} or Ti-C-O species.⁴⁵

Another observation made in literature, but lacking a complete explanation, is the deviation of the lattice parameter of bulk TiC_x . A lattice expansion can be observed in several studies, and is sometimes interpreted as tension in the coating material but is usually left uncommented.^{22, 27-29, 41} Both these issues are addressed in the present thesis, and a common explanation is suggested. A new application field for the nc- $\text{MeC}_x/\text{a-C}$ nanocomposites is also explored: Electrical contact coatings where the rare combination of electrical conductivity and wear can be utilised.

Ternary systems

By introducing an additional transition metal in the Ti-C system a ternary system is formed, and new possibilities in coating design emerge.³⁷ One of these possibilities is the formation of metastable solid solutions, structurally similar to the well-known $(\text{Ti}_{1-x}\text{Al}_x)\text{N}$ which is extensively utilised in industrial coatings.⁴⁶

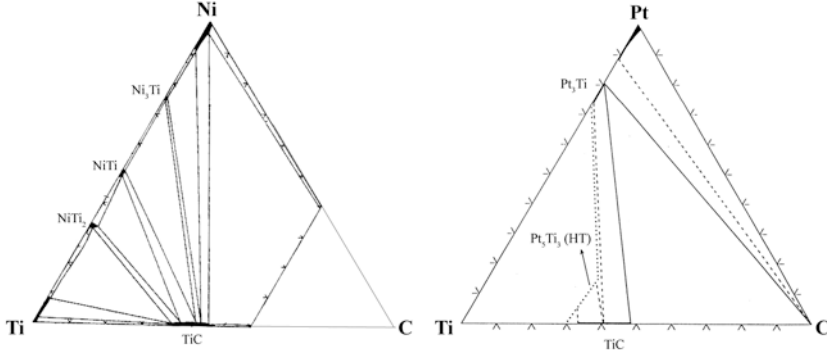


Figure 2.5 Ternary phase diagrams of Ti-Ni-C (900°C) and Ti-Pt-C (1500°C). Adapted from references 47, 48.

In the present study the alloying has been performed using late transition metals (c.f. page 15), in order to influence the bonding in the carbide phase in TiC_x . Henceforth Me will denote an arbitrary, weak carbide forming transition metal. As an example of the equilibria conditions in such systems ternary phase diagrams of the Ti-Ni-C and Ti-Pt-C (two of the systems studied in the present thesis) are shown in Figure 2.5. As can be seen, the thermodynamically stable solubility of Me in TiC_x is commonly very small, below 1 at.%. Although it has experimentally been found that solid solution carbides of strong and weak carbide forming metals, i.e. $(\text{Me},\text{Me})\text{C}_x$, can be formed with a much higher solid solubility than predicted from thermodynamical equilibrium.⁴⁹⁻⁵² This can once again be explained by the fact that some deposition methods (e.g. sputtering) are carried out at low temperatures, far from equilibrium. How far from equilibrium the sputter process can be, is indicated by the temperature quenching rate of $\sim 10^{12}$ K/s which is experienced by the atoms as they reach the growing surface.⁵³ Such supersaturated solid solution carbides of strong and weak carbide forming metals, in the present case $(\text{Ti}_{1-x}\text{Me}_x)\text{C}_y$, will have weaker average bond strengths, and will be metastable with regards to decomposition. Two decomposition processes can be considered:



The energetics involved in these processes are schematically shown in Figure 2.6, and discussed below. Decomposition (2.1) is the thermodynamically stable decomposition. The second decomposition reaction (2.2) is driven by the formation of strong C-C bonds, compared to the weak Me-C bonds. These two decompositions require different types of diffusion. Reaction (2.1) requires substitutional diffusion, which generally has a higher activation energy than interstitial diffusion, which is required for reaction (2.2).⁵⁴ In the case of MeC_x compounds the activation energy (E_A) for substitutional diffusion generally is almost twice as large (Ti in $\text{TiC}_{0.97}$, 738 kJ/mol) as for interstitial diffusion (C in $\text{TiC}_{0.97}$, 400 kJ/mol).¹² This leads to a diffusion coefficient several decades higher for the C atoms compared to Me. Hence, the thermodynamically less favourable decomposition (2.2) still may occur if the amount of available energy is insufficient for substitutional diffusion of Me. It should although be noted that Me due to the weaker Me-C bond is likely to diffuse somewhat faster than Ti. If the carbon-content of the metastable carbide is large (i.e. $y > 1-x$) the thermodynamical stable decomposition will also lead to some segregation of carbon phase.

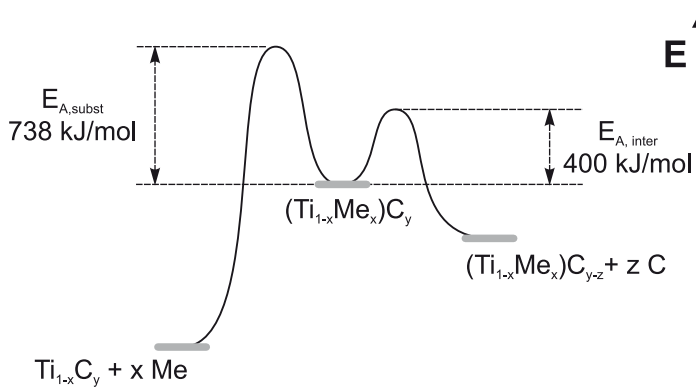


Figure 2.6 Sketch of the energetics involved regarding the two possible decomposition processes of metastable supersaturated solid solution carbides. Stated E_A values are for Ti and C in $\text{TiC}_{0.97}$ and taken from King.¹²

Besides leading to a metastable solid solution phase (the usefulness of which is discussed below) alloying the binary system of carbon and a strong carbide former (e.g. Ti) is also expected to modify the phase equilibria. The low-temperature decomposition (2.2) suggests that carbon vacancies will stabilise $(\text{Ti}_{1-x}\text{Me}_x)\text{C}_y$. It is hence expected that the upper limit of carbon-content in the carbide decreases as a result of Me-alloying. An as-deposited nanocomposite coatings $(\text{Ti}_{1-x}\text{Me}_x)\text{C}_y$ / a-C should hence have a larger amount of a-C phase than a TiC_y /a-C nanocomposite with the same total carbon-content.

The destabilisation of the TiC_x -phase by a solid solution can be used in post-deposition treatments for materials design. The decomposition processes (2.1) and (2.2) can modify the material during an annealing, forming either more carbon-phase or an additional metallic phase. Both the as-deposited enhancement of a-C, and annealing has been demonstrated in the Ti-Fe-C system by Wilhelmsson et al.⁵²

Another possibility is that the low-temperature decomposition (2.2) can be induced by the addition of external energy during use of the coating, e.g. in a mechanical contact. In a sliding mechanical contact, extra formation of free carbon phase can lead to an easily sheared graphitic carbon tribofilm and thereby a reduction of the friction, thus making such a coating self-adaptive. This has recently been demonstrated by Wilhelmsson et al. and Lindquist et al., who synthesized low friction Ti-Al-C solid solution carbides.⁵⁵⁻⁵⁷ Alloying with Al^\dagger was found to promote the formation of a free carbon phase, both during deposition and upon later mechanical sliding.

The choice of alloying element will of course give different destabilisations of the TiC-based solid solution carbide, and hence different driving forces for decomposition and modification of phase ratios during deposition. The choice of Me can also influence the result of the high-temperature decomposition. It is well known that some metals, e.g. Ag, easily segregate to the surface of carbon-based coatings.^{58, 59} This is not the case for all metals. A recent study by Stojanka et al. has shown that Fe during annealing segregates to a position inside the coating.⁶⁰ This difference is in line with the segregation energies for different metals in TiC calculated by Hugosson.⁶¹ It was found to be highly favourable for Ag, but unfavourable for Fe to segregate to the surface. Thus, depending on the choice of Me and annealing conditions it should be possible to design coatings with Me crystallites either within or on the surface of the coating.

In the research leading to the present thesis, the above design concepts were tested for several materials system. The possible formation of super-saturated solid solution carbides and the effect of alloying on the micro-structure and phase composition was investigated. The usefulness of alloyed nanocomposite coatings was also tested by determination of mechanical and electrical properties for the coatings.

[†] Although not a transition metal Al is a weak carbide former, forming the saline carbide Al_4C_3 .⁹

3. Electrical contact resistance

An electrical contact is a separable junction between two electrical conductors, which is intended to carry an electrical current or voltage. General electrical contact theory can be found in several references.⁶²⁻⁶⁵ Below, a brief overview on the main factors influencing the resistance of an electrical contact is given.

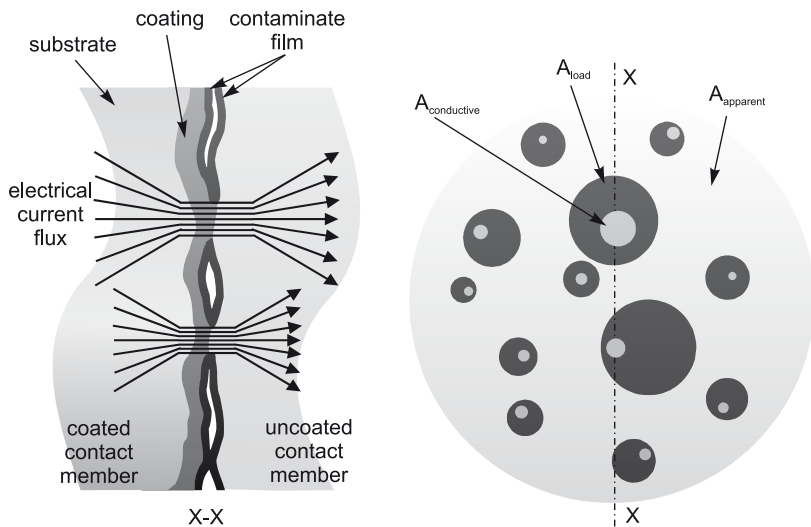


Figure 3.1 Schematics of a contact interface of a coated and an uncoated contact member. Left, a cross-section perpendicular to the contact surfaces (section X-X) showing how current is constricted to discrete points as it passes through the contact interface. Right, a cross section in plane with the contact surfaces, showing apparent area ($A_{apparent}$), load bearing area (A_{load}) and conductive area ($A_{conductive}$).

When two surfaces are pressed together physical contact only occurs at discrete spots. These are called a-spots. The number, size and distribution of the a-spots are determined by the mechanical properties of the materials in contact. The contact situation is illustrated in Figure 3.1. Mechanical contact is only achieved in parts of the apparent contact area, the load bearing area (A_{load}). The load bearing area is determined by the mechanical force in the contact, and the properties of the materials in contact. In its simplest approximation (which is considered very good for metals) the load-bearing

area (A_{load}) is calculated from the hardness of the softest material ($H_{softest}$) and the contact force ($F_{contact}$):

$$A_{load} = F_{contact} / H_{softest} \quad (3.1)$$

This area is most commonly not fully conductive, but is limited by a surface oxide layer. Since surface oxides generally are highly isolating, their influence is generally considered as a reduction of the conductive area compared to the load-bearing area: $A_{conductive} < A_{load}$, as shown in Figure 3.1. To which degree this surface oxide is broken through is also an effect of the mechanical properties of the materials in contact and their chemical properties which determines the thickness and hardness of the oxide. The penetration of the surface oxide will also be dependent on the contact force, but not in such straight forward manner as A_{load} .

The efficiency of the contact as a current conductor is determined by the resistance over the junction, the so-called contact resistance ($R_{contact}$). The primary cause of the contact resistance is that the electrical current is constricted to flow through the contact spots, causing a resistance known as the constriction resistance ($R_{constriction}$). The constriction mainly depends on two factors, the electrically conductive area and the distribution of contact spots. A wider distribution leads to a smaller constriction.

For coated connectors the resistance of the coating ($R_{coating}$) will also play a role. But for thin coatings that are less conductive than the substrate (as the case in the present work) it can be approximated that the constriction only takes place in the substrate. This means that $R_{constriction}$ and $R_{coating}$ are independent. The coating at each a-spot can be treated as a cylindrical conductor, and the total resistance of the coating can be described as:

$$R_{coating} = \rho_{coating} \cdot d_{coating} / A_{conductive} \quad (3.2)$$

where $\rho_{coating}$ and $d_{coating}$ are the coating resistivity and thickness, respectively. The contact resistance can thus be written as the sum of two contributions:

$$R_{contact} = R_{constriction} + R_{coating} \quad (3.3)$$

For sub-micron coatings with reasonable conduction $R_{constriction}$ is expected to be totally dominant.

4. Methods

The research leading to the present thesis has been experimental. Through collaborations the experimental work has been supported by theoretical simulations. Synthesised material was characterised with regards to composition, microstructure and morphology. This has been done using several different techniques, detailed below, and sometimes in collaboration with other researchers and institutes. The properties of the synthesised materials were evaluated, also partly done in collaboration with other researchers, mainly using standard techniques.

The author has personally synthesised the vast majority of the samples, and performed most of the analysis. Transmission electron microscopy, soft x-ray and ion beam methods as well as mechanical and tribological testing was mainly performed by other researchers in collaboration with the author.

Magnetron sputtering

In all cases materials have been synthesised using the physical vapour deposition technique known as sputtering. The principal of the process is sketched in Figure 4.1 (left). Sputtering is performed in a high (or ultra high) vacuum chamber where a plasma is created from an introduced gas, usually Ar. Ions in the plasma are accelerated towards a target by an applied voltage. When the ions hit the target, atoms from the target material are knocked out and can be deposited onto a substrate to form a thin film. This phenomena was first described in literature by Grove in 1852.^{66, 67}

The variant of sputtering used in this thesis is magnetron sputtering, which utilises magnets placed behind the targets to trap electrons close to the target and increase the plasma density. In this case the whole unit of target, target holder and magnets is called a magnetron. The material flux from the target has been controlled through how large current is allowed to pass through the magnetron. If a direct current (dc) is used, the process is called dc magnetron sputtering. By either using a target consisting of several elements, or using several elemental targets samples, of varying composition can be deposited.

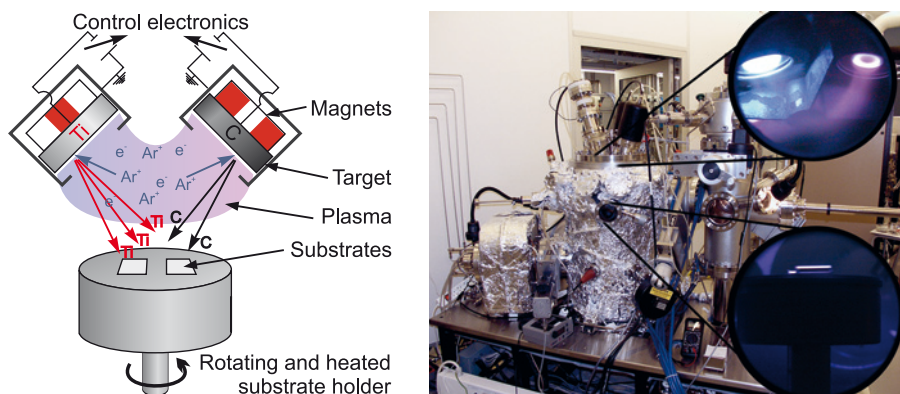


Figure 4.1 Left, a sketch of a co-sputtering process from Ti and C targets. Right, photo of the magnetron sputtering deposition system used in this thesis, named “Svanslös”. Insets showing, top: Ti and Ni targets (C target partly visible bottom left) and plasma; Bottom: substrate holder with cylinders for contact resistance measurement during deposition.

The growth process, and hence sample composition and microstructure can be influenced by events occurring both during the transport of material (atoms and ions) from the targets to the substrate, and by the conditions at the substrate/coating surface. The transport of deposition material from target to substrate is mainly influenced by gas phase scattering. The two experimental parameters which can be altered to influence this are pressure at which the deposition is performed (usually in the mTorr range) and the distance between target and substrate (usually a few to tens of cm). An increase of any of these parameters will lead to increased gas phase scattering. The gas phase scattering mainly influences the stoichiometry of the coatings, but also changes energy of the species arriving at the growing film, which can influence the coating morphology.

At the substrate the growth is mainly controlled by the possibility of (or lack thereof) the incoming atoms and ions to migrate to an equilibrium position, i.e. the surface diffusion. The surface diffusion can be increased by substrate temperature, or by applying a negative potential to the substrate, a so called bias. This will cause an ion bombardment of the growing material, causing an increase surface diffusion both by momentum transfer to surface species and local heating. The possibility of incoming species to reach an equilibrium position is also an effect of the incoming flux, i.e. how long time a surface species allowed to migrate before its position is fixed by new arrivals. Hence the deposition rate is also influencing the coating structure. Furthermore there is also the possibility of atoms on the growing surface to be re-sputtered by incoming energetic particles.

The crystalline structure of the substrate can also influence the growth. Certain crystal structures and growth directions of the growing film can be stabilised by the choice of substrate. A film which has totally ordered cry-

stalline growth compared to the substrate is called epitaxial. The prerequisites for epitaxial growth are that the structural misfit between the substrate surface and growing film is small enough and that surface migration is large enough to allow adatoms to find equilibrium positions.^{67, 68}

In the present work samples deposited at three different locations using three different sputter systems are used. The majority of samples have been synthesised in the system, which is described below and shown in Figure 4.1 (right). Samples from the two other systems have been made available through collaborations and details on these systems are given in papers **II** and **IV**.

The deposition system used in the present work is based on a UHV system with a base pressure of $5 \cdot 10^{-10}$ Torr. Three separate 2" targets with individually controlled currents were used to deposit coatings. The substrates were heated by a resistive heater placed below the substrate holders. In the present work temperatures up to 450°C were employed. Temperature was monitored by a thermoelement placed between heater and substrates, the readout of which was calibrated by pyrometer measurements of a single phase TiC sample on sample holder. Deposition time was controlled by placing a shutter just above the samples, preventing the material flux to reach the substrates. Custom machined sample holders with a 3" diameter allowed substrates of various shapes and sizes to be used simultaneously

Targets used in the above described sputter system were in general elemental and supplied by Kurt J. Lesker Company Ltd and with purities specified between 99.9 and 99.999%. Non-elemental targets were used when magnetic metals (i.e. Ni) was deposited. In this case a segmented target design with C and Ni were used in order to enable the magnetic field from the magnetron to reach the plasma and not be contained in the target material, see Figure 4.2.

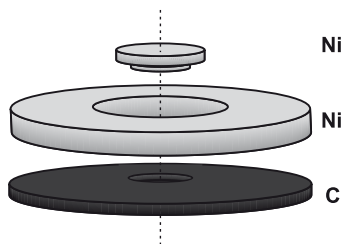


Figure 4.2 Segmented target design used for Ni-sputtering. The centre part (shown on top) can be removed to reduce the total sputter yield from the target, which was done in the present work. Outer part is clamped by target holder, middle part is fastened by the magnetic field of the magnetron. The segmented Ni-target is visible to the right in top inset in Figure 4.1 (right).

To synthesise coatings with desired compositions an iterative process of depositing calibration samples and tuning of deposition parameters was employed. Once proper deposition parameters had been determined, coatings were simultaneously deposited on appropriate substrates to allow different characterisations. Thin, single crystalline or amorphous substrates were generally used for microstructural characterisation, and metallic generally for property assessment. Highly ordered epitaxial thin films were only deposited on crystalline α -Al₂O₃(001) substrates.

Microstructural and chemical characterisation

To attain a full picture of the microstructure of a nanocomposite, several techniques which analyse different aspects of the material are often required. Below, the used methods are presented. More detailed descriptions are given for the two main analysis methods; briefer descriptions are given for other methods.

X-ray photoelectron spectroscopy (XPS)

XPS is based on the photoelectric effect. In XPS the kinetic energy of the ejected photoelectron is analysed, and the electron binding energy (E_b) is calculated. The electron binding energy is specific for each element and orbital, thus enabling elemental identification. In addition the exact binding energy is influenced by the chemical bonding in which the element participates. This makes it possible to obtain chemical information from XPS spectra.^{69, 70} In the present study, most chemical information is obtained from the C1s region. Relevant peak positions, as found in the literature, are given in Table 4.1.

Chemical composition is determined by relative peak intensities, corrected by experimentally determined sensitivity factors. In the present study, depending on the availability of reference samples or measurements, either custom-calculated or standard sensitivity factors from the instrument manufacturer were used. Since XPS analyses photoelectrons, the mean free path of the electron in matter will determine the analysis depth. With standard X-ray sources utilizing AlK α or MgK α an analysis depth up to a few nm is obtained.⁷⁰ In the present work such analysis were performed on a Physical Electronics Quantum 2000 Scanning ESCA microprobe with monochromated AlK α radiation. To obtain information on the material as such, and not only the oxidized surface, one must (when using such wavelengths) hence remove the surface of a sample exposed to atmosphere. This is done by bombardment of ions (usually of noble gases, in the present work Ar)

which will sputter away the surface of the sample. Besides removing the surface this method will also introduce defects in the analysis volume which may influence the analysis. This fact is well known and has e.g. been studied for nitride systems.⁷¹ But in the field of carbides and carbide-base nanocomposites, sputter-etching has been used rather uncritically. During the research leading to the present thesis, significant influence of sputtering artefacts was observed. This led to the use of bulk-sensitive methods, and a separate study on sputter damage. Both are presented here, as background information to the main results of the thesis in chapter 5.

Table 4.1 Literature values on some electron binding energies (E_b) for XPS core-levels, which will be relevant in the thesis

Core-level	Notation	E_b (eV)	Comment	Refs
Pt4f	Pt-Pt	71.0-71.2	pure metal	72
C1s	C-Zr	281.1	pure carbide	72, 73
	C-Ti	281.6	pure carbide	72-74
	C-Nb	281.9	pure carbide	72, 73
	C-V	282.2	pure carbide	72, 73
	C-Ti*	282.5~283.5	possible interface contribution from nc-TiC a-C	see p. 18
	C-Ni	282.8~283.9	C partly bonded to Ni	72, 75-77
	C-C	284.2~285.0	different carbon phases	72, 78, 79
	C-O	286 ~ 289	Different types C-O bonds found in surface contamination	72
Ti2p	Ti-Ti	453.7~454.1	pure metal	72
	Ti-C	454.3~455.0	pure carbide, variable stoichiometry	73, 74
Ni2p	Ni-Ni	852.7~852.8	pure metal	72
	Ni-C	853.3~853.4	carbide bonding	77

Another way to increase the information depth in XPS is to increase the energy of the used X-rays. This gives larger kinetic energy of the photoelectron and hence a greater inelastic mean free path and escape depth. This method is known as high kinetic energy (HIKE) XPS or hard X-ray photoelectron spectroscopy (HAXPES).⁸⁰ HIKE XPS is today almost exclusively performed at synchrotron radiation facilities where different wavelengths easily can be selected. HIKE measurements were in the present work performed at the KMC-1 beamline at the BESSY II facility in Berlin, Germany.^{81, 82}

Even though HIKE is bulk sensitive, HIKE-spectra acquired with hard X-rays still contain considerable amount of surface information. One possible way to obtain pure bulk information is to calculate the difference between a

more and a less surface sensitive spectra. For such a subtraction to be successful and sound one must consider two things: Firstly there must be one easily identifiable region or peak which is known to originate from, and only from, surface. This region can then be used to scale the spectra, opting for a minimisation of the intensity in the region. Secondly, any difference in spectral resolution between the spectra must be compensated for. This can be disregarded if the natural width of the studied peaks is larger than the spectral resolutions involved. An example of such a calculation on the C1s region of a nanocomposite sample, using spectra obtained from 2 and 6 keV X-rays, is shown in Figure 4.3. Here the contribution from C-O bonds at ~ 289 eV were used for normalisation and the difference spectra reveal two contributions (C-Ni and C-Ti*) otherwise not identifiable. This method is presented in publication I, together with results on the influence on ion-etching on the material analysis which are presented below.

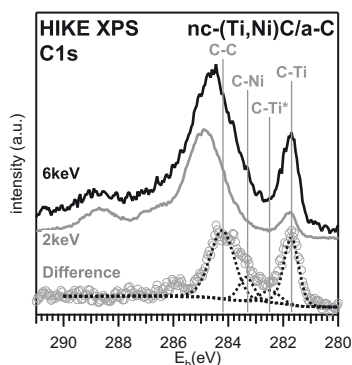


Figure 4.3 HIKE difference method illustrated with the C1s region of a nanocomposite sample from publication I.

The use of HIKE XPS and difference spectra as described above is a neat method, but it requires hard X-rays of several energies and can thus presently only be performed at synchrotron sources. This makes it impractical as a standard method. To analyse something else than the surface oxidation there are hence two choices. Either the formation of a surface oxide is avoided, which is achieved through vacuum transfer systems (none available during the present research); or the surface oxidation must be removed through sputter etching, which should be performed with care. During the analysis of coatings in the Ti-Ni-C system, substantial differences in spectra obtained after sputter etching with 500 eV and 4 keV Ar^+ was discovered.

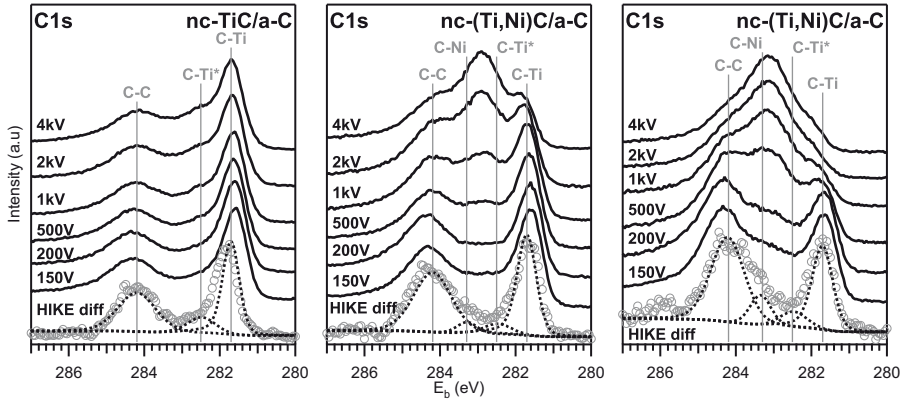


Figure 4.4 C1s spectra obtained after different sputter-etchings. Reference data in the form of HIKE difference spectra shown at bottom in grey. The different panels show spectra from three samples. The samples have varying degree Ni-alloying, and evidently different susceptibility to sputter-damage. Data from publication I.

In Figure 4.4 C1s spectra from a series of TiC-based nanocomposites with different amounts of Ni-alloying are shown. Spectra are either obtained after sputter etching to a constant depth using different ion energies (black curves); or attained by the HIKE-difference method described above (grey markers). The latter are to be considered reference spectra of the undamaged material. As can be seen, spectra in the middle and right panels exhibit a considerable influence of the ion energy. The spectra shown in the left panel, show some differences, but markedly smaller. These differences are clearly sputter damage, and are mainly visible as extra intensity at 282.6-283 eV. The use of ions with energies in the keV range does for some samples disrupt the C1s spectra to such a degree that no bonding analysis is possible. By peak fitting procedures, involving data from the HIKE reference spectra, the amount of sputter damage can be estimated. The relative amount of sputter damage in the C1s region as a function of the ion energy, for the samples in Figure 4.4 are given in Figure 4.5. The three samples are affected differently by the ion bombardment. This is due to different chemical stability. Ni-alloying causes a metastable solid solution phase, and the degree of metastability is dependent on the Ni-concentration. Details are given in papers I and VI, as well as on page 51. The effect of varying ion energies is intuitively easy: higher ion energy leads to that impinging ions reach deeper and that a larger amount of energy is deposited in the sample by each ion. The increased number of ions required to sputter the sample when the ion energy is decreased, does generally not lead to a larger amount of deposited energy. This intuitive picture has been confirmed by simulations of Ar^+ ions into TiC, see publication I.

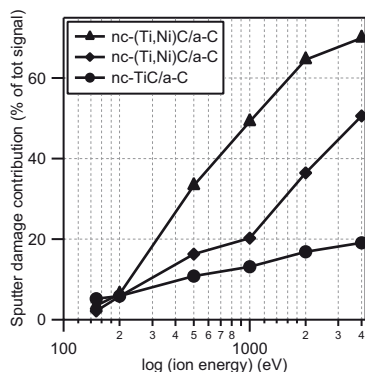


Figure 4.5 Relative amount of sputter damage in the C1s region of XPS spectra for different samples and ion energies. Data from publication VI.

The presence of sputter damage has also been shown for other solid solution carbide systems, i.e. Ti-Pt-C, Ti-Al-C, Ti-Cu-C and Ti-Fe-C systems. Hence it has been proven that this is a more general issue, not isolated to one materials system. This also implies that much of the published analysis based on high resolution XPS spectra obtained after sputter etching may be erroneous. This is especially true for any analysis of nanocomposite systems containing metastable phases. The above results clearly show that consideration of possible sputter damages must be taken into the analysis of carbide based nanocomposites. For the above shown samples, and other samples in the present work, Ar^+ energies of 150 or 200 eV should be sufficiently low to allow bonding analysis, as long as one is aware of the presence of sputter damage and limits conclusions accordingly.

X-ray diffraction (XRD)

XRD can be used to detect and analyse crystalline phases. The method uses coherent scattering of X-rays that have wavelengths in the same order of magnitude as the lattice planes in a crystalline structure. From the diffraction pattern (diffractogram), which exhibits peaks at discrete angles, the crystal structure and lattice parameter can be determined via Bragg's law.⁸³

The peak broadening (excluding instrumental broadening) in diffractograms has two main causes, a non-infinite crystalline domain (i.e. crystallite size) and distortion of the crystalline lattice (i.e. strain). As a first approximation (which is valid if there is no strain contribution to the broadening) the crystallite size can be estimated by Scherrer's equation.⁸³ A slightly better approximation can be given by the Williamson-Hall method, which separates the size and strain contributions. This method requires more than three diffraction peaks to yield reliable results, and can hence not be used for all samples in the present study. Even more complex methods which should give more accurate results exist, but require a large number of diffraction

peaks. Even if the results from Scherrer's equation are unreliable in absolute values, they are still useful in comparing samples within a series. Trends can to a much greater extent be relied upon.⁸⁴ When not otherwise stated, grain-sizes have been estimated with Scherrer's equation.

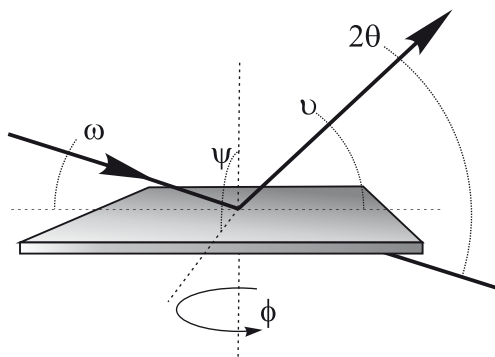


Figure 4.6 Sketch of angles and set-up for various XRD measurements. Solid shape represents the sample with coating facing upwards.

There are many different types of XRD measurements, whereof some have been used in the present work. The traditional XRD measurement with a diffractometer is the so called locked-couple[‡] measurement where incident angle ω and exit angle ν are changed with the same speed (angles are defined in Figure 4.6). Hence the diffraction angle 2θ continuously changes and diffraction is only observed from lattice planes parallel to the sample surface. For thin films it is common to use a constant, grazing incidence (GI) angle (ω). This will decrease the escape-depth of the x-rays and hence give an enhancement of the coating signal. Diffraction pattern is obtained by changing the exit angle ν and thereby the diffraction angle 2θ . This measurement will probe lattice planes of different spatial orientation, depending on the combination of ω - and 2θ angles. To determine the lattice parameter parallel to the sample surface a locked-couple measurement can be performed at a ψ -angle close to 90° . To determine the orientation of crystallites in highly ordered thin films one can perform pole figure measurements. In these measurements, the 2θ -angle is kept constant (matching a desired diffraction peak) and rotation (ϕ) and tilt angles (ψ) are varied. This will give the spatial directions of lattice plane normal, and hence the orientation of the crystallites. Combining pole-figures of diffraction angles for both coating and substrate any epitaxial relationship can be determined. In the present work XRD was performed on Bruker D5000 and Pan Analytical X'Pert MRD diffractometers, using Cu K α radiation. Different optics and set-ups were used depending on the type of diffraction measurement.

[‡] Also known as a θ - 2θ measurement, from that the incident angle sometimes is called θ and that both incident and diffraction angle (2θ) are changed during the measurement.

Other analysis techniques

Raman spectroscopy utilises a shift in wavelength of scattered light due excitation of vibrational modes in molecules or solid matter. Raman spectroscopy has in the present work been used to characterise amorphous carbon phases, and spectra are mainly evaluated as ‘fingerprints’ for different types of bonding. For these studies a Renishaw micro Raman System 2000 with 514 nm or 785 nm lasers was used.⁸⁵

Scanning electron microscopy (SEM) uses a focused electron beam and detects scattered electrons to build an image of a sample surface. SEM was performed to obtain morphological information on the surfaces and on fractured cross sections of synthesised coatings. A Leo 1550 FEG-SEM was used. Transmission electron microscopy (TEM) utilises electrons transmitted through a thin sample, which requires extensive sample preparation. From TEM one can obtain an image of the material, as well as chemical or structural information. In the present thesis mainly imaging has been used. Imaging TEM can be operated in various modes, such as scanning TEM (STEM) which provides pure z-contrast and high resolution TEM (HRTEM) which utilises phase contrast to obtain atomic resolution on crystalline samples.

Soft x-ray spectroscopic techniques include emission (SXE) and absorption (SXA) which probes occupied and unoccupied electron states, respectively. These measurements were performed at the I511-3 beamline at the MAX-lab synchrotron facility in Lund, Sweden.

One techniques used to determine the surface structure of samples are low energy electron diffraction (LEED). LEED utilises diffraction of electrons to investigate ordered surface structures. These are detected and analysed by a diffraction pattern and results are an average over a large surface.

X-ray reflectivity (XRR) was performed on calibrations samples to determine their thickness and thereby calculate appropriate times for later depositions. XRR was performed on a Bruker D5000 diffractometer with Cu K α -radiation. Elastic recoil detection analysis (ERDA) was used to calibrate some sensitivity factors used in XPS. In ERDA, high energetic ions (in the present case 40 MeV $^{127}\text{I}^{8+}$) are used to bombard the sample, and recoiling ions from the sample are detected. From energy and mass of the recoils the chemical composition as a function of depth can be calculated without the use of any sensitivity calibrations.

Assessment of properties

The electrical resistivity of coatings was determined by the well established four-point-probe method. This method gives the sheet resistance, which if multiplied by the thickness of the thin film gives the resistivity.^{86, 87} For all such measurements coatings deposited on isolating substrates (α -SiO₂ or α -Al₂O₃) were used.

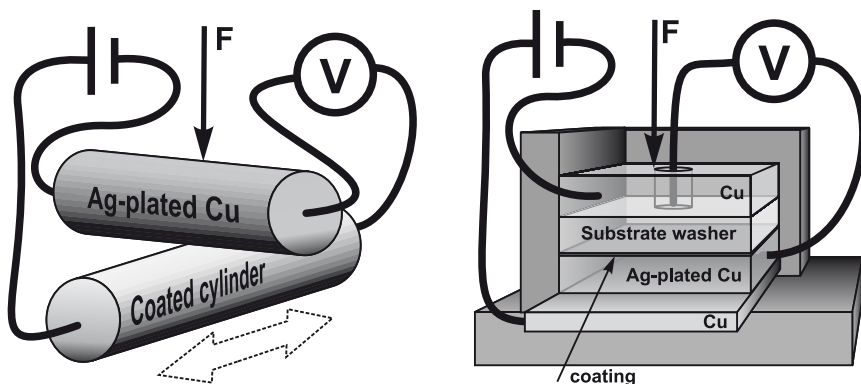


Figure 4.7 Sketch of contact resistance set-ups. Left, the crossed cylinders set-ups. For the static measurements cylinders are fixed so that they cannot twist or turn in any direction. For sliding measurements the bottom cylinder moves according to the arrow. Both voltage and current cables directly inserted into cylinders. Right, flat washer set-up. Voltage cables in direct contact with back-side of substrate, and inserted into counter contact. Current collected through separate Cu-platens (top and bottom).

The contact resistance was determined as a function of contact force. Three set-ups were used: One static and one moving crossed cylinder set-up; as well as one static washer set-up, see Figure 4.7. The washer set-up mimics an application, while the crossed cylinder set-up shown is a pure lab set-up. During a measurement a constant current is passed over the contact junction and the voltage drop over the contact is measured with a voltmeter. In all measurements the counter contact was Cu coated with Ag.

The hardness (H) and Young's modulus (E) of selected samples were determined using nanoindentation. In this method the depth of a diamond tip which is pressed into the material is followed as a function of force. H is given as the ratio of the peak load and the load carrying area. E is obtained from the slope of the unloading curve, according to the method presented by Oliver and Pharr.⁸⁸ In the present work, Berkovich tips were used and indentations were performed with a Nanoindenter XP or a CSM Ultra nano hardness tester.

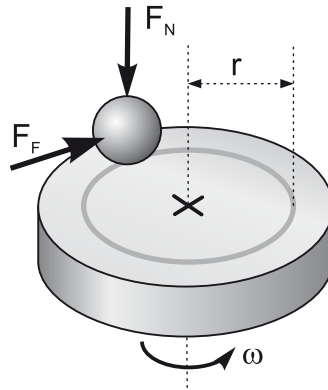


Figure 4.8 Set-up for ball-on-disc friction test

The tribological properties of selected coatings were determined by the common lab-scale ball-on-disc test. In this set-up, shown in Figure 4.8, a ball is pressed against a rotating disc and a sliding contact is achieved. In the present work, coated disc and uncoated steel balls were used. From this type of measurement coefficient of friction is determined as the ratio of the frictional force and the normal force on the ball F_N/F_F . One can also compare life-time and wear of coatings tested under identical conditions. Deeper tribological understanding is attained by analysis of wear tracks on both ball and disc.

Theoretical modelling

Theoretical simulations of solid state compounds can assist experimental work in several ways. By being faster than experiments, simulations can easily scan through potentially interesting materials system and compositions. And thereby aid in selecting promising candidates for further experimental studies. Simulations are also valuable in explaining experimental observations by providing information on how, e.g., bonding structure varies, something which can be difficult to obtain a clear picture of experimentally.

In so called *ab initio* methods one wants to calculate the state of a system without using prior experimental knowledge. This essentially means solving the Schrödinger equation, but an exact analytical solution only is possible for a one-electron system (i.e. the hydrogen atom). To study other systems one must hence use approximations and use numerical methods. The different approximations and numerical methods are most often evaluated by comparing to experimental data, and a suitable method is chosen with regards to the system studied. Hence, very few simulations are fully independent of experimental data, even though no experimental data are given as parameters. Experimental solid state systems have far too many electrons (in the

order of 10^{23}) to be studied in simulations. To perform simulations on crystalline solids one instead performs calculations on a limited number of atoms in a so called super cell and employs periodic boundary conditions, creating an infinite and periodic surrounding.^{89, 90}

In the present work simulations of solids were performed using density functional theory (DFT). This method is based on the hypothesis that knowledge of the spatially dependent electron density of the ground state for any electronic system uniquely determines the system, and especially the ground state total energy. DFT methods do hence not attempt to explicitly solve the Schrödinger equation, but to calculate the spatially dependent electron density. The simulations primarily yield the spatially dependent electron density and the electronic energy of the system. The energy makes it possible to study relative stabilities of different configurations or compounds. The electron density makes it possible to study the bonding structure through looking at electron density maps, or calculating the density of states (DOS).

5. Results

The central question of the research in the present thesis has been the correlation between composition, microstructure and morphology on the one hand, and properties of the materials on the other hand. The work has been performed in an exploratory manner, by varying experimental parameters (primarily the composition of the material) and observing what microstructure and phase composition is obtained, and by correlating this to observed properties. The research has solely been devoted to carbide-based materials with a focus on TiC_x -based materials and nanocomposites. Some research has also been performed on pure carbide material, although most as support to the nanocomposite research.

Binary Me-C materials

Attention has been given primarily to the Ti-C system, where the work with the present thesis has generated many samples and much data. Some samples have also been produced in the V-C, Nb-C and Zr-C systems. The compositions of samples have been chosen so that carbides or nanocomposites of carbide and amorphous carbon have been obtained. Pure metal or carbon samples have only been synthesised as reference materials, and no samples containing metal and carbide phases have been produced.

Carbides and nanocomposites in the Ti-C system

Coatings in the Ti-C system were deposited in several studies, both for possible applications as low friction and/or electrical contact coatings (see properties page 61), and for fundamental research. Papers **II** through **V** are dedicated to this system, but some results also appear in other papers. Samples were deposited with different stoichiometries and under slightly different conditions. All samples with a high enough (varies with experimental conditions such as temperature and bias) carbon-content were found to be two-phased nanocomposites. This is illustrated in Figure 5.1 where TEM images of a nanocomposite sample are shown. In the STEM image (left) the particle phase can be seen to have a higher average Z-value (bright contrast) than the surrounding matrix; in the HRTEM image (right) the particles are found to

have an ordered (crystalline) structure, whilst the matrix phase has a disordered (amorphous) structure. In Raman spectroscopy, typical spectra from an sp^2 -rich amorphous carbon (a-C) phase is observed, see Figure 5.20 (bottom, left).

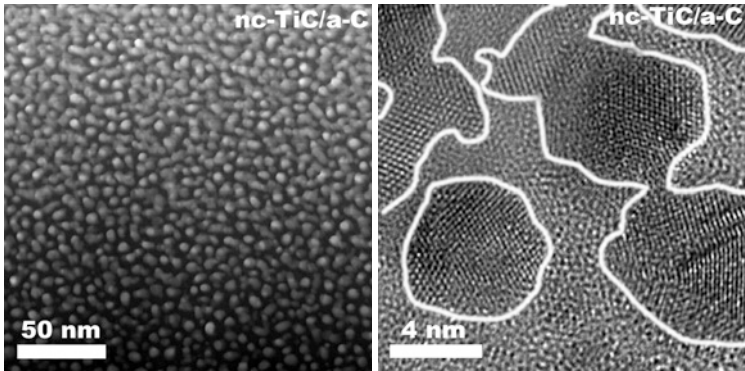


Figure 5.1 Planview STEM (left) and HRTEM (right) images of a nanocomposite nc-TiC/a-C sample with a total carbon content of 52 at.%. White lines mark outlines of crystalline regions observed in HRTEM.

From XRD (see Figure 5.2, left) the ordered phase is found to be TiC. In XPS of the C1s region (Figure 5.2, right) one can identify clear peaks of C-Ti bonds (from the crystalline TiC-phase) and C-C bonds (from the a-C phase). The third component (C-Ti*) is also due to C-Ti bonds and is described in detail below (page 41). As the total carbon-content of the samples increase the relative amount of a-C increases, see Figure 5.2 (right). This will lead to a greater separation of the crystalline TiC-grains. Coupled with this is also a decrease in grain size, seen by peak broadening in Figure 5.2(left). For the sample series shown in Figure 5.2, the variations as a result of different composition are summarised in Table 5.1.

Table 5.1 Data on the series of TiC-samples shown in Figure 5.2, where the composition has been varied. [C] denotes total carbon content as determined from XPS sputter depth profiles. a and r are the lattice parameter and grain size from XRD. C-C, C-Ti* and C-Ti are relative intensities of contributions to the C1s XPS spectra shown in Figure 5.2 (right). x is the stoichiometry of the TiC_x phase.

Sample	[C] (at.%)	a (Å)	r (nm)	C-C (%)	C-Ti* (%)	C-Ti (%)	x in TiC_x
1	35	4.334	17	7	14	79	0.50
2	42	4.348	11	24	16	60	0.55
3	51	4.365	8	40	16	44	0.61
4	65	4.375	3	66	16	18	0.63
5	100	-	-	100	0	0	-

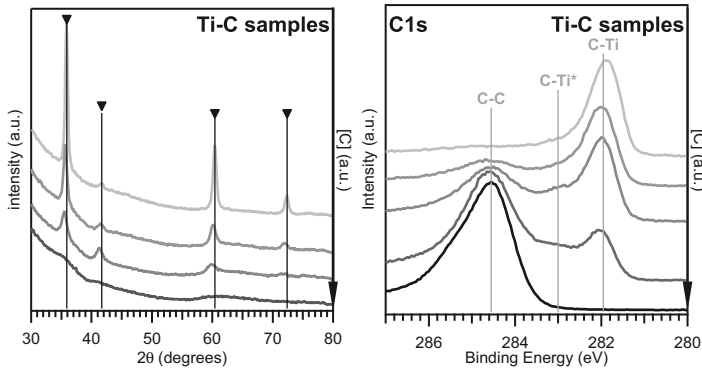


Figure 5.2 Diffraction patterns (left) and XPS C1s spectra (right) from a series of Ti-C with samples of varying composition. Carbon-content increases downward in both graphs, see Table 5.1 for values. XPS spectra attained after sputter-etching to a depth of 150Å with 200eV Ar⁺ ions. ▼ in left panel show reference positions for bulk TiC.⁹¹ Data from publication **III**.

The combination of total carbon content and the ratio of carbon bonded in respective phases leads to the conclusion that the carbide phase must be substoichiometric, i.e. TiC_x. This is also shown in Table 5.1 where it can be seen that x increases with total carbon-content, but TiC_x never reaches a fully stoichiometric composition. This illustrates the non-equilibrium conditions of sputter deposition. How far deposited coatings are from equilibrium can be controlled by a number of experimental parameters, such as substrate temperature or bias. The latter is illustrated in Figure 5.3, where samples of almost constant composition are shown to have different amount of a-C phase, as a result of different substrate biases. A summary of XRD and XPS results for this series is given in Table 5.2, where the two main effects of the bias voltage are illustrated. When bias is increased, energy is provided to the growing surface and conditions approach thermodynamical equilibrium, i.e. the carbide phase becomes less substoichiometric, and less a-C phase is formed. At the same time the ions that bombard the growing material introduces defects and disturbs the growth process, i.e. the grain size decreases.

Table 5.2 Data on the series of TiC-samples shown in Figure 5.3. Columns show same things as in Table 5.1.

Bias	[C] (at.%)	a (Å)	r (nm)	C-C (%)	C-Ti* (%)	C-Ti (%)	x in TiC _x
0 V	53	4.363	10	27	13	60	0.81
-50 V	51	4.362	13	22	11	67	0.82
-100 V	51	4.387	10	21	14	65	0.83
-200 V	51	4.424	5	16	17	67	0.87

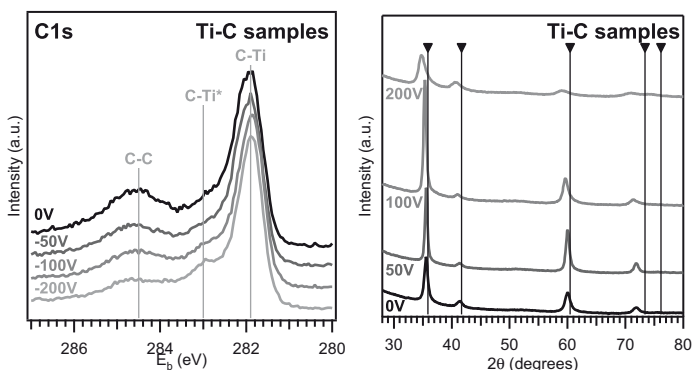


Figure 5.3 XPS C1s spectra of four samples with almost the same total carbon-content (51-53 at.%), but different applied substrate biases. XPS spectra attained after sputter-etching to a depth of 150Å with 200eV Ar⁺ ions. ▼ in right panel mark reference positions for TiC.⁹¹

Two general observations can be made regarding the change in coating morphology and appearance as carbon content increases. All samples show a metallic finish. Samples without a-C phase have a light grey colour. As the amount of a-C increases samples become successively darker and the reflectivity diminishes slightly. The morphological evolution of the coatings is illustrated in Figure 5.4, where cross sections of one nc-TiC_x (left) and two nc-TiC_x/a-C (right) coatings are shown. As can be seen there is a columnar growth, which gradually becomes less pronounced as carbon-content increases. In the columns of the two nc-TiC_x/a-C samples there is also a graininess in the columns which agrees with the grain sizes determined from XRD. Columnar growth is common when low substrate biases are used. Except for the bias-series above, only low bias voltages have been used to obtain coatings discussed in this thesis. The columnar growth is hence a general observation for the coatings synthesised in the present work.

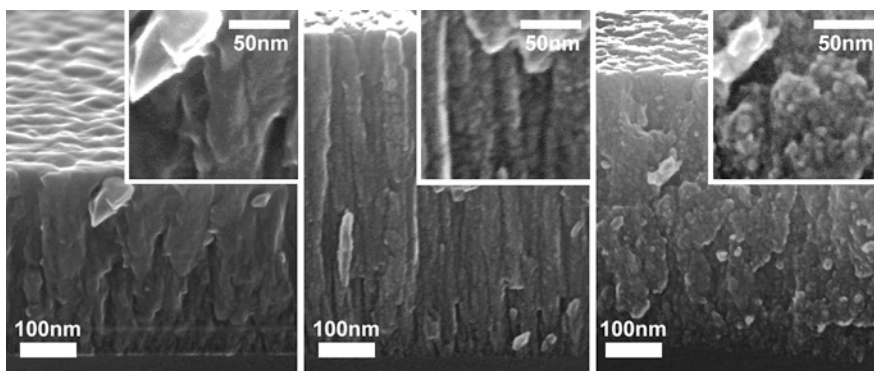


Figure 5.4 Fractured cross sections of Ti-C coatings observed in SEM. From the left total carbon-content of the samples are 36 at.%, 54 at.% and 68 at.%, respectively.

The experimental results suggest that the nc-TiC_x/a-C nanocomposite is not simply a mixture of a-C and nc-TiC_x. In Figure 5.5 HIKE difference spectra are shown for one pure TiC_x-sample and three nanocomposite nc-TiC_x/a-C samples. For the nanocomposite samples a third spectral component (C-Ti*) is required to fit the observed spectra. The relative intensity of C-Ti* compared to C-Ti varies between samples and the ratio $C-Ti^*/C-Ti$ is generally found to be larger for samples with smaller grain-size.

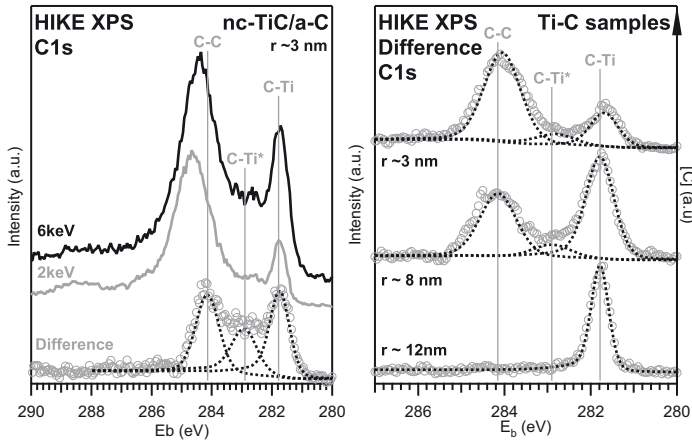


Figure 5.5 HIKE-difference spectra of the C1s region from nc-TiC_x/a-C nanocomposite samples. Bulk-sensitivity hence attained without the use of sputter-etching, Left, raw and difference spectra for a single sample. Right, difference spectra for a series of samples with varying composition: one pure carbide sample (bottom) and two nanocomposites.

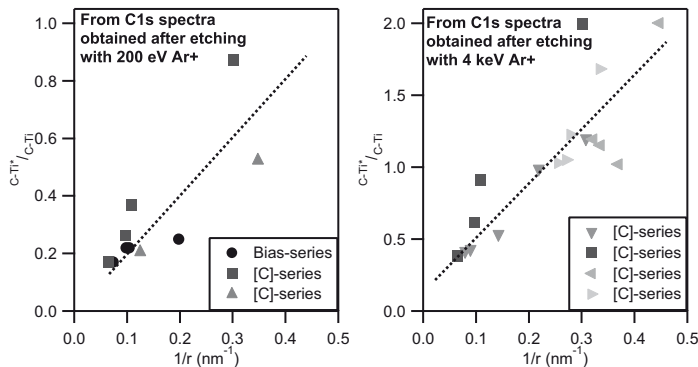


Figure 5.6 Correlation of C-Ti* contribution to C1s XPS spectra with the inverse grain size for several series of Ti-C samples. Left panel with values obtained from spectra after sputter-etching using 200eV Ar⁺ ions and right spectra from spectra after sputter-etching with 4keV Ar⁺ ions, which hence contain more sputter damage. Note different y-scales. Dotted lines are only guides to the eye.

As has been noted above (page 29), these types of coatings are sensitive to sputter damage, and this damage manifests itself as intensity around the position of the C-Ti* contribution. This means that XPS data obtained after sputter etching may be unreliable with regards to C-Ti*. Still the trends visible in Table 5.1 and 5.2 with an increased ratio C_{Ti^*}/C_{Ti} are notable. To illustrate this, the ratio C_{Ti^*}/C_{Ti} has been plotted over the inverse grain size ($1/r$) in Figure 5.6. As can be seen there is a clear correlation between the C-Ti* bonding state and the inverse grain size, which is consistent with a contribution from the surface of the TiC_x particles.

There are hence strong indications that the C-Ti* contribution to the C1s spectra originates from the interface between the nc- TiC_x and a-C phases. This is schematically illustrated in Figure 5.7. As the grain size decrease, the relative amount of interface increases. Also the observed binding energy of the C-Ti* is consistent with a interface contribution. Carbon atoms at the interface will have fewer Ti nearest neighbours than carbon atoms in the bulk of TiC_x , and hence a smaller total charge transfer to these C atoms is expected, leading to a smaller chemical shift. One of the previous suggestions on the origin of C-Ti* (see chapter 2, page 18) was given by Kuznetsov et al.,⁴³ who proposed that C-Ti* originates from $Ti_{14}C_{13}$ clusters. In these clusters there are two types of carbon, one with bulk-like surroundings, and one at the surface. Hence this can be considered a special case of our more general explanation of C-Ti* as an interface state. It was also proposed that oxygen bonding could be involved.⁴⁵ Although a few atomic percent oxygen is present in the studied coatings, there is (in contrast to the grain size) no general correlation between the oxygen-content and C-Ti*.

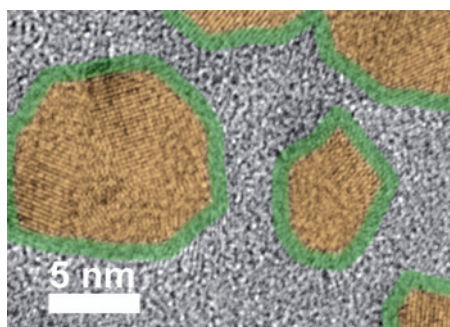


Figure 5.7 Schematic picture based on a HRTEM image of a nc- TiC_x /a-C nanocomposite. Green areas mark a 1nm thick interface region, yellow mark the rest of the TiC_x crystallites. As can be seen the relative amount of interface increases drastically as grain size reaches a few nm.

Further evidence for different bonding is found in the valence band, as observed by XPS, see Figure 5.8. In the left panel a change in valence band spectra can be observed as the total carbon content changes. In the right panel one can clearly see that spectra of the nanocomposite (circles) not can

be explained as a superposition of the spectra of a-C and nc-TiC_x references (dotted lines). This indicates that the chemical bonding in the nanocomposite significantly differs from the pure materials. According to Didziulis et al.⁷⁴ the region where the nanocomposite shows decreased intensity (~1 eV) represents interaction of C2p and Ti3d orbitals in the TiC_x phase. The region about 7 eV, shows an increased intensity indicating additional states, this is more pronounced as grain size decreases and hence once again consistent with a contribution from the interface between TiC_x and a-C phases. In TiC, the region ~7 eV consists of bonds involving C2p, Ti4p and Ti4s orbitals, this must although not be the case for an interface state.

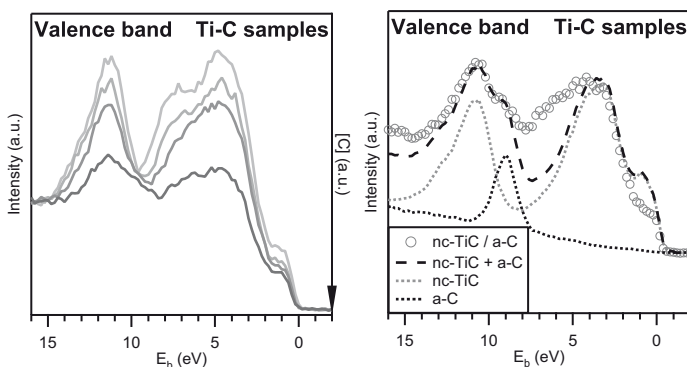


Figure 5.8 The valence band region from XPS measurements. Left a series of nc-TiC/a-C samples (also shown in Figure 5.2 and Table 5.1). Right an attempt to fit the spectra from a nc-TiC/a-C sample with those from nc-TiC and a-C spectra. Spectra attained after sputter-etching to a depth of 150Å with 200eV Ar⁺ ions.

Soft X-ray absorption and emission (SXA and SXE) studies presented in publication **III** also indicate a different bonding in the nanocomposite compared to nc-TiC_x and a-C samples. It was observed that the number of occupied Ti3d states decreased and the number of occupied C2p states increased as grain size decreased.[§] This hence shows an increased charge transfer from Ti3d to C2p orbitals as TiC grain size decreases. This charge transfer could occur within the TiC_x phase, but more likely it occurs across the interface TiC_x | a-C which represents a larger portion of the carbide phase as grain size decreases. An increased ionicity of the Ti atoms was also observed, which could be the effect of a net charge transfer from TiC_x. Due to metallic Ti3d-3d σ overlap in the TiC_x-phase (see Figure 2.3) a net charge-transfer at the interface region is likely to be spread out over the entire crystal. For large

[§] This is hence the observation from SXE. Consistent observations from SXA, that the number of unoccupied Ti3d states increased and that the number of unoccupied C2p states decreased, was also made.

crystals the charge deficiency hence becomes negligible. For nanoscale crystals on the other hand, this charge deficiency could due to the relatively larger amount of interface be relevant.

To attain more details on the potential interface bonding, difference spectra were calculated for the C K SXE (see Figure 5.9). Here scaled reference spectra from nc-TiC_x and a-C samples have been subtracted from spectra of three different nanocomposite samples. As can be seen, there is for all four excitation energies an increase in intensity as grain size decreases. This is consistent with the behaviour of an interface contribution. Specifically it was found that the nanocomposite had broken Ti3d e_g-C2p bonds, and additional Ti3d t_{2g}-C2p bonds. The former is consistent with the decrease in XPS valence band just below the Fermi-level commented above; while the latter can be connected to the increased intensity in the XPS valence band ~7eV.

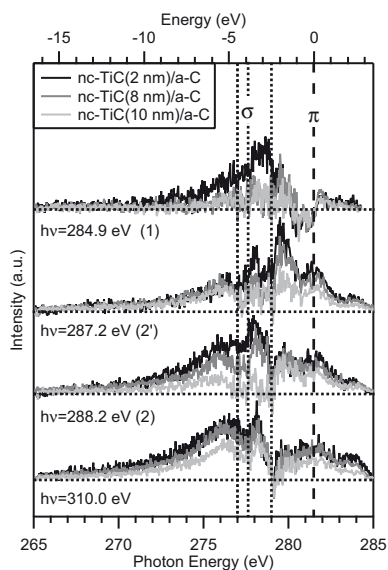


Figure 5.9 Difference spectra from SXE excited at different energies. Scaled a-C and nc-TiC_x spectra have been subtracted from nc-TiC_x/a-C spectra (different shades of grey). Adapted from paper III.

As can be seen from Table 5.1-2 the cell parameters of TiC_x in the nanocomposite are significantly larger than literature values for bulk TiC_x, 4.30-4.33 Å.⁹² This has also been observed in literature, c.f. chapter 2, page 18. Furthermore, the results suggest a correlation to grain size where the smallest grains exhibit the largest cell axis, see Figure 5.10. A lattice expansion for small TiC_x grains has been reported earlier. Fukuhara showed good agreement between calculated and observed lattice expansion for isolated nanoparticles, although this expansion were much smaller than those observed here.⁹³

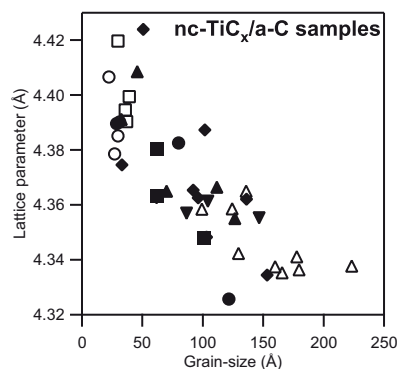


Figure 5.10 The variation of lattice parameter as a function of grain size for several series of Ti-C samples of varying total carbon content. Solid markers for series synthesised by the author, open marker for series made available through collaboration.

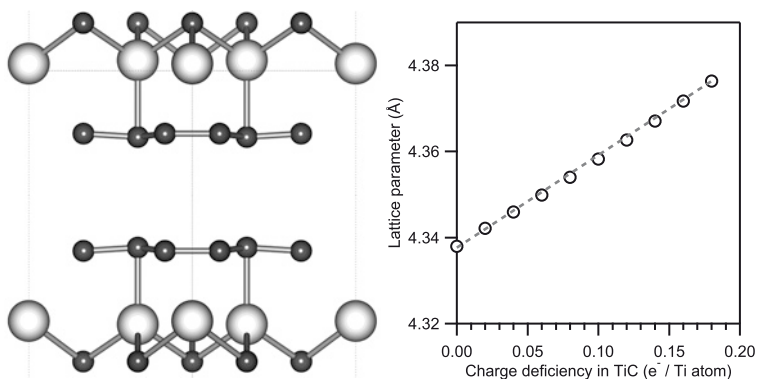


Figure 5.11 Left, part of the model used to simulate the interface between TiC and C. Actual simulation box has more TiC-layers than shown. Right, the calculated lattice parameter for TiC as a function of e^- -deficiency.

A possible explanation for the lattice expansion can be the charge-transfer across the nc-TiC_x | a-C interface proposed above. To investigate this, theoretical simulations were performed.⁹⁴ The charge-transfer was investigated using a model of the (111) surface with carbon on top, see Figure 5.11 (left). The simulation slab consisted of two atomic layers of graphite between a total of 12 atomic layers of TiC. Since the van-der-Waals bonding between the graphite layers is difficult to reproduce with DFT the interlayer distance was fixed, and the LDA approximation was used. These calculations showed an average net charge-transfer of 0.11e V per C atom at the interface. This charge was transferred from Ti atoms at the TiC surface to C at the interface. This is a considerable charge-transfer, and indicates that the interface bonding indeed is different. Even if the charge transfer across the interface is considerable, the total charge transfer to the C atoms at the interface is

smaller than for C in the TiC bulk. The main reason for this is the reduced number of Ti neighbours at the interface. The effect of a charge-transfer across the $\text{TiC}_x \mid \text{a-C}$ interface was investigated by other simulations; using electron-deficient TiC simulated using the virtual crystal approximation (VCA). Geometry optimisation yielded results presented in Figure 5.11 (right). As can be seen the lattice parameter of the electron-deficient TiC phase was found to increase as a function of electron deficiency. This hence supports the observed lattice expansion has its origin in a charge-transfer across the $\text{nc-TiC}_x \mid \text{a-C}$ interface and thus is a feature of the nanocomposite. Even though these simulation may not be a perfect representation of reality (other surfaces of TiC as well as other positions for C can be relevant), they still show that a charge-transfer across the interface can occur and that an electron-deficient TiC would expand. Together with experimental data this makes a convincing argument for a distinctly different interface bonding, which includes a considerable charge-transfer.

In summary, it has been shown that the nanocomposite $\text{nc-TiC}_x/\text{a-C}$ is more complicated than a pure mixture of the included phases. Additional bonding states exist. They show a strong correlation with the grain size of the carbide phase, as expected for an interface state. This is also confirmed by theoretical simulations. Consistent theoretical and experimental results together thus suggest that this interface bonding incorporates a significant charge-transfer from Ti3d states in the carbide to C2p states at the surface of the carbide. This charge-transfer causes a lattice expansion in the carbide. A significantly different interface bonding will most probably have an effect on properties of the material, such as electrical or thermal conductivity; and could be part of the explanation of the superhardness which in some cases has been observed for $\text{nc-TiC}_x/\text{a-C}$ nanocomposites.^{25, 32}

Up-scaling / industrialisation of Ti-C coatings

To produce coating material in industrial scale, the type of sputtering mainly used in the present research (co-sputtering from elemental targets in UHV-system), is undesirable. To make a method economical, simpler systems and higher throughput is required. This is mainly achieved by two changes to the deposition process: the use of a single compound or composite target, and higher deposition rate. Industrial processes are hence quite different those used in paper I-IV. This means that the moving of materials synthesis from research to industrial scale often requires additional research or development, so called up-scaling. To investigate the up-scaling of the $\text{nc-TiC}_x/\text{a-C}$ synthesis, a series of Ti-C coatings were synthesised in industrial scale equipment (see paper V). In this study the effect of two deposition para-

meters (deposition pressure and target to substrate distance) on sample microstructure and performance was investigated. In general it was found that coatings with comparable microstructure (see Figure 5.12) and performance (see below, page 61) to laboratory scale coatings could be produced.

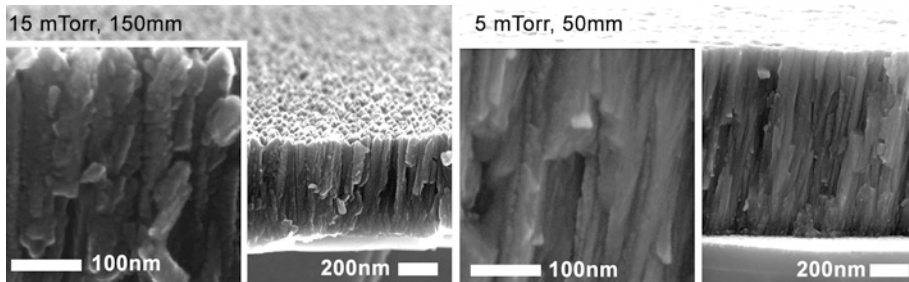


Figure 5.12 SEM images at two magnifications of two fractured cross section. Samples were deposited at different pressures and target distances from the same target. Left 15 mTorr, 150 mm. Right 5 mTorr, 50 mm.

However, it was observed that the deposition pressure and the target-substrate distance influenced the composition and chemical bonding. This is exemplified in Figure 5.13 (left), where C1s XPS spectra of two coatings deposited from the same target are shown. Firstly, it is clear that the coatings are deficient in carbon compared to the 1:1 stoichiometry of the target material, see Figure 5.13 (right) where triangular markers show the C_{Ti} ratio increasing with larger target distances. This suggests that the pressure-distance conditions used in these depositions affect the larger Ti atoms to a higher degree than the smaller carbon atoms. Hence the differences in mean free path must play an important role in the process. The carbon deficiency is contradictory to results in literature, both for sputtering from segmented TiC/C-targets by Stüber et al. and Pei et al.,^{23, 24} and in the similar system Ti-Si-C,⁹⁵ where an excess of C is generally observed and mainly explained by a smaller degree of scattering for the smaller and lighter C atoms. Furthermore, the increase of the carbon content with increased target distance is also contradictory to the results of Eklund et al.,⁹⁵ where an increase in metal content was observed as pressure-distance was increased. Since no plasma diagnostics were performed a complete explanation cannot be given, but one probably important factor is the target material. In the present study a two phase (graphite and Ti metal) composite target was used, in the above references targets with only or large parts of compound material (TiC, TiC/C and Ti_3SiC_2) were used. The chemical bonding in these two cases are substantially different and may give differences in energy and angular distribution of ejected particles, as well as preferential sputtering effects.

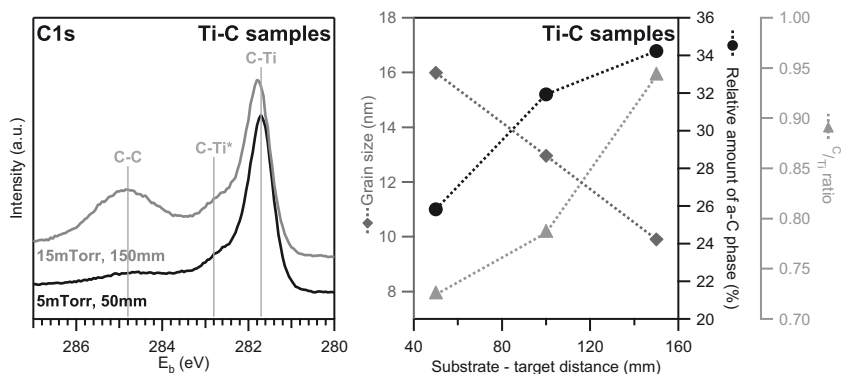


Figure 5.13 Left, C1s XPS spectra of two coatings deposited in industrial scale equipment. Spectra were obtained after sputter etching with 4 keV Ar^+ ions. Right, illustration of the effect of pressure-distance conditions in the industrial scale deposition: stoichiometry, amount of free carbon and grain size as a function of substrate to target distance for samples deposited at 15 mTorr. Data from paper V.

The other differences in coating microstructure can be explained by a higher degree of gas phase scattering at higher pressure and / or longer distances. This will cause lower adatom mobility, which will lead to a less kinetically hindered growth. A coating microstructure closer to thermodynamical equilibrium is thus formed: in this case, a less substoichiometric TiC_x and less formation of the a-C phase, see Figure 5.13 where an example is shown in the left panel and the trend is illustrated in the right panel (● markers). Consistent with a lower adatom mobility is also the observation that grain-size decrease with target distance (and deposition pressure), see Figure 5.13 (right), ♦ markers.

Nanocomposites in the V-C, Zr-C and Nb-C systems

A few samples were also deposited in other binary systems. It was then found that nanocomposites could be formed in a similar manner to what is observed in the Ti-C system. Figure 5.14 shows XPS and XRD results from three samples in the V-C, Zr-C and Nb-C systems. Carbide phases are identified in XRD,⁹⁶⁻⁹⁸ and as can be seen, there are contributions from free and carbidic carbon in all three XPS spectra. The peak positions match references for respective carbide, see Table 4.1. The presence of a third peak (C-Zr*) similar to C-Ti* is noted in the spectra of the Zr-C. The lack of such a peak in the V-C and Nb-C samples is probably due to the smaller chemical shift in these cases. Grain sizes were found to be in the order of 3 to 9 nm, which is fully comparable to Ti-C samples synthesized under similar conditions. Raman (not shown) also reveals the typical signature spectra of a-C. TEM micrographs (not shown) of the Nb-C sample also confirm the nanocomposite microstructure. Since no series of samples with varied conditions

or composition were produced no detailed investigations similar to the ones described above were conducted. These results do although show that synthesis of nc-VC_x/a-C, nc-ZrC_x/a-C and nc-NbC_x/a-C is possible, which increases the degrees of freedom available for materials design of carbide based nanocomposites.

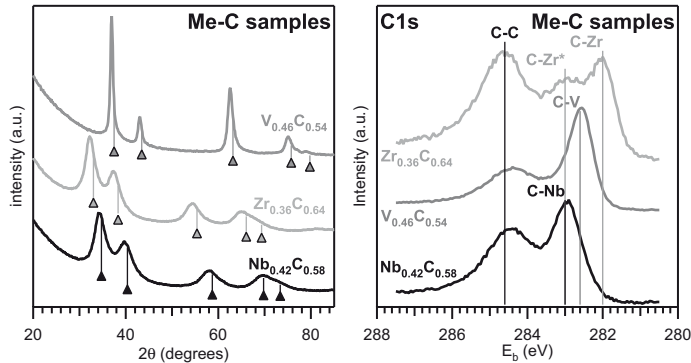


Figure 5.14 XRD (left) and XPS (right) of nanocomposite samples in the V-C, Zr-C and Nb-C systems. Stoichiometries state total compositions. Reference positions of respective carbide MeC_x is marked with ▲.⁹⁶⁻⁹⁸

Alloying Ti-C: ternary Ti-Me-C materials

As was discussed in chapter 2 (page 19) there is a possibility for weak carbide forming metals, such as Al or Fe, to form solid solutions in carbides of strong carbide formers under non-equilibrium synthesis conditions. It has also been shown that such metastable solid solution carbides can be useful both due to spontaneous decomposition during use,^{52, 55-57} and as precursor material for design of nanostructures through annealing.⁶⁰ To investigate these concepts further, both experimental and theoretical studies were initiated. In the theoretical studies, the alloying of TiC with all other 3d transition metals was investigated. The experimental studies were limited to three ternary systems based on Ti-C, where the carbide forming abilities of the alloying metal was varied: Ti-Ni-C, Ti-Pt-C and Ti-Cu-C. Ni is a weak carbide former, and only metastable carbides are known. Pt is an even weaker carbide former, and synthesis of PtC has only been reported under extreme conditions.¹⁴ And finally, Cu is a non-carbide former. No carbide phases of Cu are known.

In the experimental work, samples were generally deposited in several series with (roughly) constant carbon content and varying degree of alloying. In the studied systems, at least one series was based on a single-phase TiC_x sample (in the non-alloyed case), and at least one series was based on a nc-TiC_x/a-C nanocomposite sample (in the non-alloyed case).

Theoretical results

The stability of ternary TiC-based solid solution carbides, $(\text{Ti}_{1-x}\text{Me}_x)\text{C}_y$, were investigated for $\text{Me} = \text{Sc}, \text{V}, \text{Cr}, \text{Mn}, \text{Fe}, \text{Co}, \text{Ni}, \text{Cu}$ and Zn with $x = 0.25, 0.50, 0.75$ and 1.0 . Simulations were performed using super cells specially adapted to simulate disordered solutions. The energy of formation was calculated according to the following equation:

$$E_{\text{Form}} = E(\text{Ti}_{1-x}\text{Me}_x\text{C}_1) - \{ (1-x) \cdot E(\text{Ti}) + x \cdot E(\text{Me}) + (1-y) \cdot E(\text{C}) \} \quad (5.1)$$

The results are presented in Figure 5.15(left), where a negative energy hence represents a thermodynamically stable solid solution. The $(\text{Ti}_{1-x}\text{Sc}_x)\text{C}_y$ and $(\text{Ti}_{1-x}\text{V}_x)\text{C}_y$ phases were found to be stable regardless of x , which is in agreement with phase diagrams. In the other systems the solid solutions becomes metastable for some alloying concentration. As expected from general bonding trends (c.f. chapter 2, pages 14-15) the later transition metals give larger destabilisation of the solid solution. In Figure 5.15 (right) the energy for the carbon segregating decomposition (2.2) on page 19, is calculated according to:

$$\Delta E_{\text{segregation}} = E(\text{Ti}_{1-x}\text{Me}_x\text{C}_{1-0.25}) + 0.25 \cdot E(\text{C}) - E(\text{Ti}_{1-x}\text{Me}_x\text{C}_1) \quad (5.2)$$

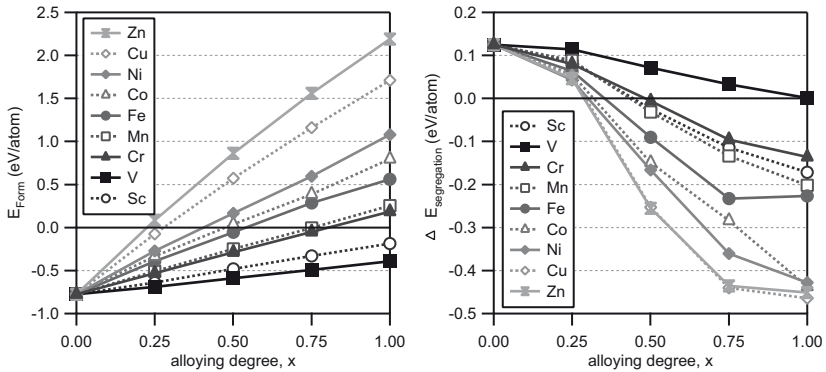


Figure 5.15 Formation energy (left) for the solid solution carbides $(\text{Ti}_{1-x}\text{Me}_x)\text{C}$; and (right) the energy for carbon segregation according to (5.2). Negative energies signify thermodynamically stable solid solutions (left), and that decomposition through segregation of C is favourable (right), respectively.

As can be seen, the segregation energy is negative (i.e. segregation is favourable) above a certain alloying content x for all alloying elements except V. This shows that the proposed low-temperature decomposition of super-saturated solid solution carbide through interstitial diffusion of carbon will lower the total energy of the system. This decomposition should hence be dominant when the available energy is insufficient for any significant rate of substitutional diffusion.

The destabilisation of the solid solution carbide can be explained with the same reasoning as the general trend in carbide stability: the filling of anti- and non-bonding states as valence electron concentration increases, c.f. chapter 2, pages 14-15, specially Figure 2.1 (right).

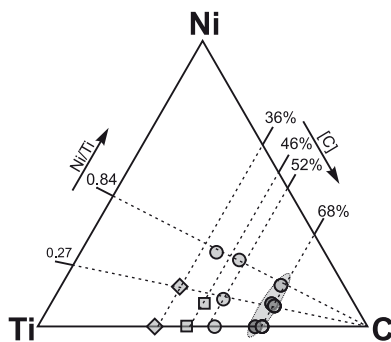


Figure 5.16 Nominal composition of the samples in the Ti-Ni-C system. Different markers for different microstructure types in samples: ◇ for single-phase polycrystalline carbides, □ for epitaxial carbides (deposited at higher temperature) and ○ for nanocomposites. The sample series used to illustrate results of as-deposited coatings marked with a grey area. Samples used in annealing experiments have darker markers.

Ti-Ni-C materials

From Figure 5.16 it can be seen that Ti-Ni-C coatings were deposited in three series with different carbon content. All ternary samples have a Ni-content above the thermodynamical solubility limit of Ni in TiC_x (< 1 at.%).⁴⁷ Samples were produced to investigate the Ti-Ni-C system, and the possible application of coatings as low friction and / or electrical contact materials. Coatings were deposited at 300°C to a thickness of $0.5\text{-}1.0\ \mu\text{m}$ and relevant properties evaluated, see page 61. Below, details will be given on the phase- and microstructure of one of the sample series (marked by a grey area in Figure 5.16), which illustrates the observed influence on microstructure. The studies on as-deposited Ti-Ni-C coatings are detailed in paper **VII** and **VIII**.

Diffractiongrams and XPS spectra of the C1s region from the carbon-rich nanocomposite sample series are shown in Figure 5.17. As can be seen from the diffractiongram (left), the only observed crystalline phase matches the pattern of TiC_x . There are two distinct changes as Ni is introduced: Firstly, there is a systematic shift of diffraction peaks towards higher diffraction angles, which is consistent with a decrease in lattice parameter as can be expected if Ni ($r_{\text{met}} = 1.25\ \text{\AA}$) substitutionally replaces Ti ($r_{\text{met}} = 1.45\ \text{\AA}$). Secondly, a peak broadening can be observed. This is interpreted as a decrease in grain size (3 to 2 nm), something which generally is observed upon alloying of carbide-

based materials.⁴⁹⁻⁵² The XPS spectra, Figure 5.17 (right), shows a clear influence of the Ni-alloying: The relative amount of a-C phase increases drastically. This is consistent with the decreased stability of a super saturated solid solution carbide $(\text{Ti}_{1-x}\text{Ni}_x)\text{C}_y$, and consequent shift in carbon-content of the carbide, c.f. chapter 2, page 19, and Figure 5.15 (right). Not distinguishable in these XPS spectra (due to lack of spectral resolution and sputter damages), but observable in the HIKE reference spectra of the medium carbon-content Ti-Ni-C series in Figure 4.4, is a C-Ni contribution at 283.4 eV.

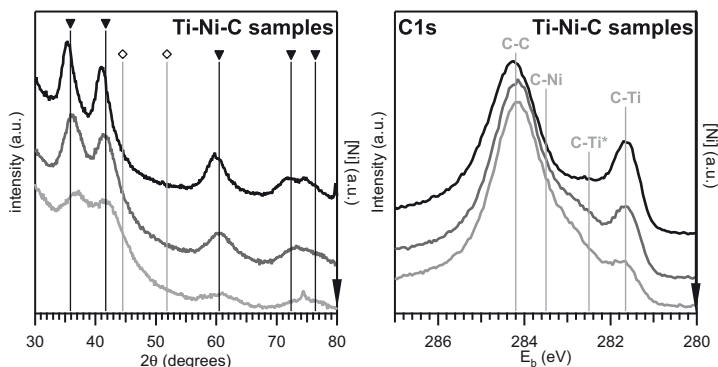


Figure 5.17 XRD (left) and XPS (right) of the carbon rich Ti-Ni-C sample series. Ni-content increases downward in both graphs. Markers in left panel mark reference positions for TiC (▼) and Ni (◇) phases.^{91, 99} XPS spectra were acquired after sputter etching to a depth of $\sim 150\text{\AA}$ using 200 eV Ar^+ ions.

That C and Ni form chemical bonds in the material is confirmed by XPS spectra of the $\text{Ni}2p_{3/2}$ region, see Figure 5.18 (left). The main peak is shifted to a higher binding energy which is consistent with Ni-C bonds.⁷⁷ Also, the well known Ni-satellite is shifted, from +5.2 eV to +7.2 eV from the main peak. This is consistent with Ni participating in a non-metallic bond.¹⁰⁰ The valence band region, Figure 5.18 (right), also shows a large influence of the Ni-alloying. The region just below the Fermi level exhibits a largely increased intensity. This region mainly contains contributions from $\text{Me}3d$ and $\text{C}2p$ orbitals.^{74, 101} Since Ni has four times as many d-electrons as Ti, this increased intensity is consistent with Ni substitutionally replacing Ti in the TiC_x lattice.

The nanocomposite structure of these samples is confirmed by TEM, see Figure 5.19 where micrographs of binary and Ni-alloyed nanocomposites are shown. It is clearly visible how the increased amount of a-C matrix phase leads to grain separation and less columnar growth. Micrographs with higher magnification also confirm the decrease in grain size from 2-4 nm in the binary case, to 1-3 nm in the most alloyed case (particles visible in Figure 5.19 bottom, right are polycrystallites).

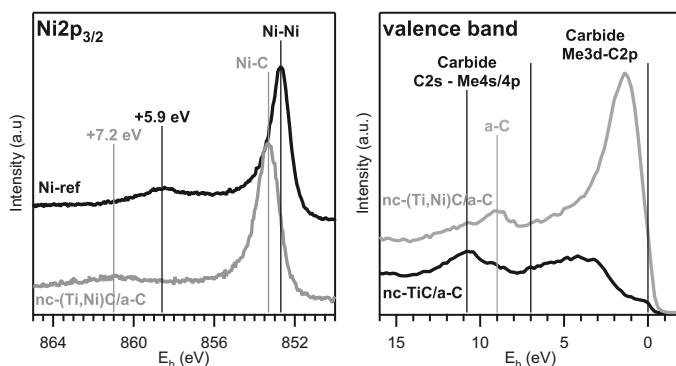


Figure 5.18 XPS of the $\text{Ni}2p_{3/2}$ (left) and valence (right) regions for alloyed $\text{nc}-(\text{Ti}_{1-x}\text{Ni}_x)\text{C}_y/\text{a-C}$ nanocomposites (in grey) and references in black (Ni metal and binary nanocomposite, respectively). Samples in right panel have a carbon-content of 66-68 at%. Spectra were acquired after sputter etching to a depth of $\sim 150\text{\AA}$ using 200 eV Ar^+ ions.

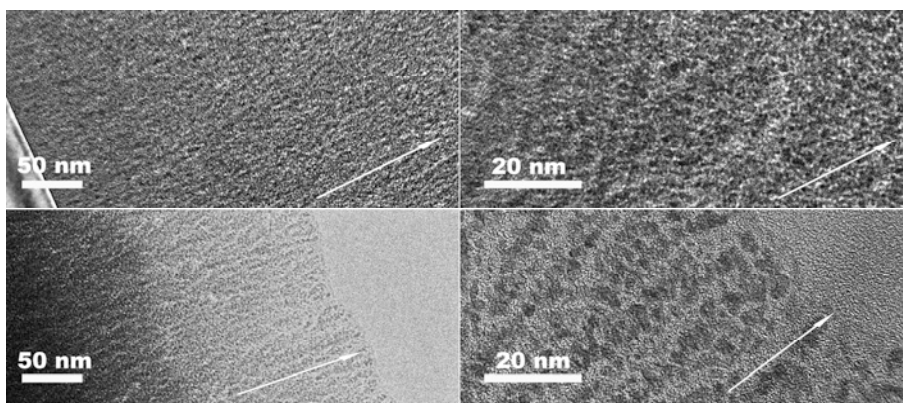


Figure 5.19 TEM-images of a binary nc-TiC/a-C nanocomposite (top) and a ternary $\text{nc}-(\text{Ti}_{1-x}\text{Ni}_x)\text{C}_y/\text{a-C}$ nanocomposite (bottom). Samples have comparable carbon content (68 at% and 66 at.%, respectively). Coating growth direction indicated by arrows. XRD and XPS of these two samples are shown in Figure 5.17 (top and bottom).

It is hence concluded, that the $(\text{Ti}_{1-x}\text{Ni}_x)\text{C}_y$ supersaturated solid solution carbide can be formed, and that the alloying of nc-TiC/a-C coatings with Ni will lead to changes in the microstructure, in agreement with predictions in chapter 2. In particular it was found that the relative amount of a-C phase in the as-deposited material increased as a result of the alloying. This can be utilised for materials design. The solid solution $(\text{Ti}_{1-x}\text{Ni}_x)\text{C}_y$ was not only observed in nanocomposites, but also synthesised in phase pure samples, both in polycrystalline (see paper VII) and epitaxial form (see page 67). Determination of the lattice parameter in, both in- and out-of-plane, for the latter confirms the reduction of lattice parameter as a result of the solid solution of Ni in TiC_x .

To confirm the proposed decomposition mechanism (see page 19) for the solid solution carbide $(\text{Ti}_{1-x}\text{Ni}_x)\text{C}_y$ additional annealing experiments were carried out. These were conducted on the binary and ternary samples shown with darker marks in Figure 5.16. Annealing experiments were performed in a vacuum furnace ($p = 1 \cdot 10^{-7}$ Torr) for 20 minutes at 400°C, 600°C and 800°C, and results of subsequent analysis are presented in Figure 5.20. The differences between the two compositions in their as-deposited state, black curves, are consistent with the results above. Changes to the binary sample as an effect of the annealing were small. For the ternary sample there is a small increase of amount of free carbon also for mild annealing (400°C for 20 min and 500°C for 2 hours, dotted line). Distinct changes start to occur from 600°C, when the D- and G-peaks of the Raman spectra start to separate, indicating graphitisation, and the XRD show an increased background, possibly an early sign of Ni-nucleation. At 800°C there are very clear Ni-peaks in the diffractogram, and Raman spectra show a clear graphitisation. Additionally the peak broadening of the TiC_x diffraction peaks has decreased, indicating an increase in grain size.

Sputter depth profiles (not shown) show that the 600°C and 800°C experiments leads to a segregation of the Ni towards the substrate. This is however not connected to a change in C1s peak shape. For all annealing experiments the C1s peak has a shape independent of sputter depth. This confirms that the increase of free carbon observed in Figure 5.20 is a result of decomposition of the carbide phase, and not a segregation of the existing a-C phase towards the surface. The segregation of Ni towards the substrate does not compare with the theoretical results of Hugosson et al., where surface segregation of Ni in TiC was predicted.⁶¹ The calculated segregation energy of Ni was however close to zero which means that the driving force is small and easily affected by other factors. The fact that the present samples are nanocomposites, and that simulations were performed on single-phase carbide could hence be relevant. The results support the decomposition routes proposed above (page 19), where carbon segregation by interstitial diffusion (reaction 2.2) dominates at low temperatures, and that substitutional diffusion (reaction 2.1) requires higher temperatures. Judging from the experiment at 500°C (dashed lines in Figure 5.20) it should be possible to adjust annealing time and temperature in such a way that a considerable formation of free carbon is attained without the substantial formation of a Ni phase. It should hence be possible to design materials through choice of annealing process, and either obtain an increased amount of a-C phase, or a metallic phase (and an increased amount of a-C).

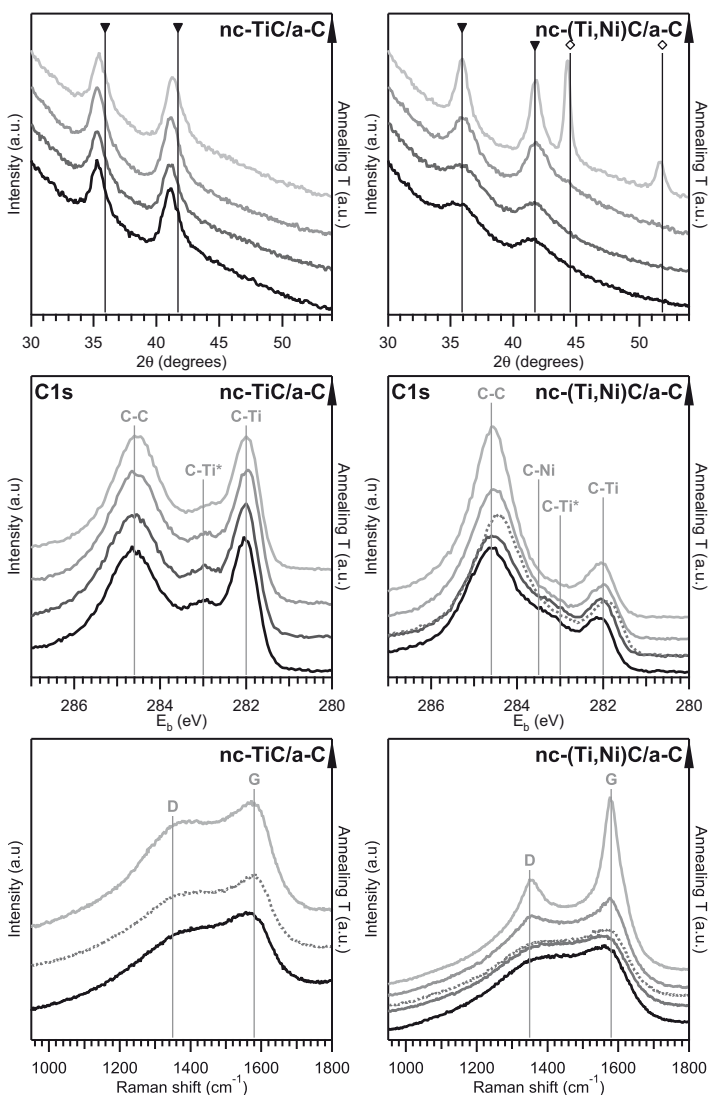


Figure 5.20 Results of annealing experiments on binary nc-TiC/a-C nanocomposite (left) and ternary nc-(Ti_{1-x}Ni_x)C_y/a-C nanocomposite (right). Top XRD, middle C1s XPS and bottom Raman. Black curves show as-deposited sample, grey curves show samples annealed for 20 minutes at 400°C, 600°C and 800°C (increasing upwards). Dotted line mark an annealing experiment conducted at 500°C for 2 hours. Markers in top graphs (diffractogram) show reference positions for TiC (▼) and Ni (◇) phases.^{91, 99}

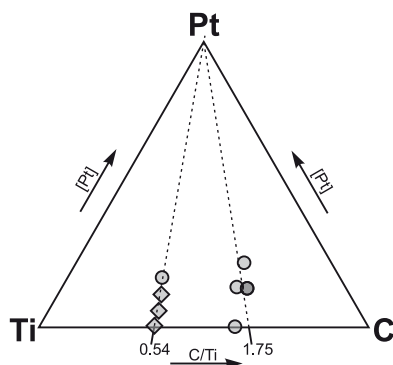


Figure 5.21 Nominal composition of the samples in the Ti-Pt-C system. Different markers for different microstructure types in samples: \diamond for single-phase polycrystalline carbides and \circ for nanocomposites. Sample used in annealing experiment has darker marker.

Ti-Pt-C materials

In the Ti-Pt-C system, samples were deposited in two series: one pure carbide and one nanocomposite, see Figure 5.21. The Pt-content of all samples exceed the solubility limit of TiC, c.f. phase diagram in Figure 2.5. The coatings were synthesised in order to investigate the material system as such and to determine if materials suitable for sensor applications could be produced. Coatings were deposited at room temperature, to a thickness of about 500 Å. The study on Ti-Pt-C is described in more detail in paper IX.

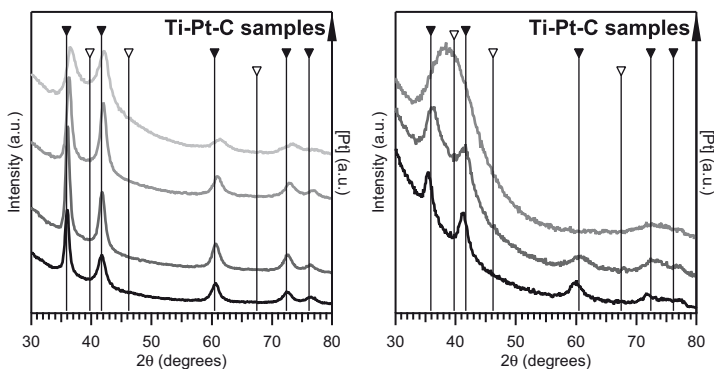


Figure 5.22 XRD from the two sample series in the Ti-C-Pt system. Composition of the samples are shown in Figure 5.21. Left panel shows Ti-rich series, right panel shows C-rich series. Markers show reference positions for TiC (\blacktriangledown) and Pt (\triangledown) phases.^{91, 102} Pt-content increases upwards in the graphs.

Figure 5.22 shows diffractograms from the two series. As in the case with the Ti-Ni-C system, generally only diffraction peaks matching TiC_x is observed, together with a systematic shift of the positions to lower angles. The latter is consistent with a substitutional solid solution of Pt ($r_{\text{met}} = 1.39 \text{ \AA}$) in the TiC_x phase, i.e. $(\text{Ti}_{1-x}\text{Pt}_x)\text{C}_y$. As can be seen there are no clear diffraction peaks from Pt, but the wide ‘peak’ in the top diffractogram of Figure 5.22 (right). This is probably the result of overlapping between wide TiC and Pt diffraction peaks. This is supported by the observation of lattice fringes in HRTEM (not shown) matching both metallic Pt and TiC.

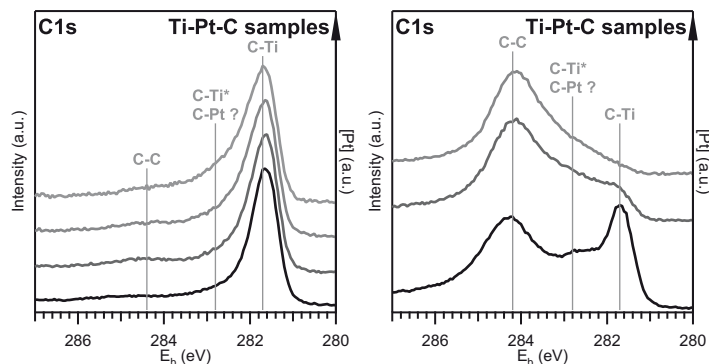


Figure 5.23 XPS of the C1s region the two sample series in the Ti-C-Pt system. Left, the carbon-poor carbide-series; and right, the carbon-rich nanocomposite series. Spectra obtained after sputter etching to a depth of $\sim 150 \text{ \AA}$ using 200 eV Ar^+ ions.

Solid solution of Pt into the carbide phase is supported by XPS-results, primarily the Pt4f peak position of $71.6\text{--}71.7 \text{ eV}$, which is substantially different from the position found in metallic Pt, $71.0\text{--}71.2 \text{ eV}$. XPS spectra from the C1s region of both sample series are shown in Figure 5.23. In spectra from the carbon-poor series (left) only carbon-metal bonds can be observed, and from the carbon-rich series (right) both C-C and C-Ti bonds are observed. Furthermore, a clear influence of the Pt-alloying can be observed in both series. For both series the intensity around 283 eV increases as a result of Pt-alloying, this is where a contribution from C partly bonded to Pt and Ti would be expected and is hence consistent with a solid solution carbide $(\text{Ti}_{1-x}\text{Pt}_x)\text{C}_y$. For the nanocomposites a change in relative amount of C-C and C-Me bonds, similar to what was observed for the Ti-Ni-C system above. This suggests that the formed $(\text{Ti}_{1-x}\text{Pt}_x)\text{C}_y$ not is a thermodynamically stable compound and is likely to decompose upon annealing, which is to be expected from the position of Pt in the periodic table and the lack of PtC_x at normal conditions. It is hence concluded that a supersaturated solid solution carbide $(\text{Ti}_{1-x}\text{Pt}_x)\text{C}_y$ can be synthesised through sputtering, both as single phase, polycrystalline material, and as a part of a nanocomposite with a-C.

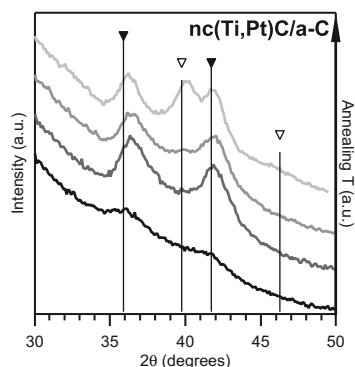


Figure 5.24 XRD of annealed $\text{nc}-(\text{Ti}_{1-x}\text{Pt}_x)\text{C}_y/\text{a-C}$ coatings. Annealing was performed for 1 hour under vacuum at 650°C , 750°C and 850°C . Temperature increases upwards in figure, diffractogram of as-deposited sample shown in black. Markers show reference positions for TiC (\blacktriangledown) and Pt (\triangledown) phases.^{91, 102}

To investigate the decomposition of the formed supersaturated $(\text{Ti}_{1-x}\text{Pt}_x)\text{C}_y$ and possible design of $\text{nc}-(\text{Ti}_{1-x}\text{Pt}_x)\text{C}_y/\text{a-C}/\text{nc-Pt}$ coatings annealing experiments were conducted. Experiments were carried out a sample in the carbon-rich series (darker marker in Figure 5.21). Annealing was performed for 1 hour at 650°C , 750°C and 850°C . XRD results are shown in Figure 5.24. As can be seen crystalline Pt forms from 750°C and above. Unlike the Ni-alloyed case no increase of a-C phase could be noted upon alloying. The only change in the C1s peak upon annealing (not shown) is the disappearance of the C-Pt bonds. This shows that the thermodynamically more favourable decomposition (2.1) (c.f. chapter 2, page 19) is fully dominant in this system. Sputter depth profiles of as-deposited and an annealed sample (Figure 5.25) also reveals a segregation of the formed Pt towards the substrate. This is similar to what was observed for the polycrystalline $(\text{Ti}_{1-x}\text{Ni}_x)\text{C}_y$. In the work of Hugosson Ni and Pt have very similar segregation

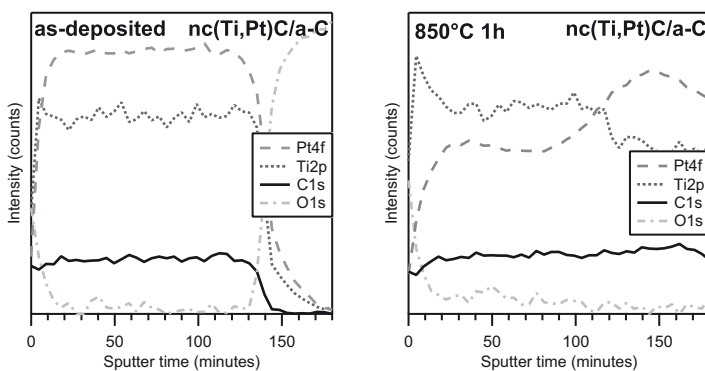


Figure 5.25 Sputter depth profiles of as-deposited and annealed $\text{nc}-(\text{Ti}_{1-x}\text{Pt}_x)\text{C}_y/\text{a-C}$ coatings. Sputter etching performed with 200 eV Ar^+ ions.

energies,¹⁰³ so a similar behaviour is not surprising. The segregation of Pt towards the substrate will probably inhibit any use of the material as a sensor, since such applications rely on catalytical Pt particles on the surface. Although not explicitly simulated in the theoretical studies, the destabilisation of TiC_x by Pt agrees with the expected trends, as commented in paper VI.

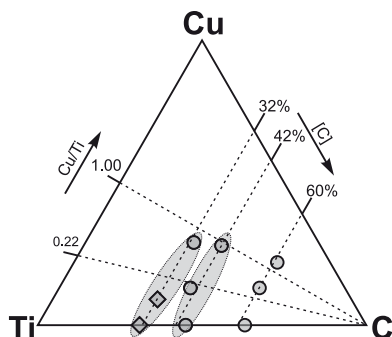


Figure 5.26 Nominal composition of the samples in the Ti-Cu-C system. Different markers for different microstructure types in samples: ◇ for single-phase polycrystalline carbides and ○ for nanocomposites. Series shown in the present work marked with grey areas.

Ti-Cu-C materials

Coatings in the Ti-Cu-C system were deposited in similar series and under the same conditions as the Ti-Ni-C samples. Composition of the samples are shown in Figure 5.26. Since no stable or metastable copper carbides are known (c.f. Figure 2.2), any solid solution of Cu in TiC is expected to be smaller than in the Ni and Pt cases.

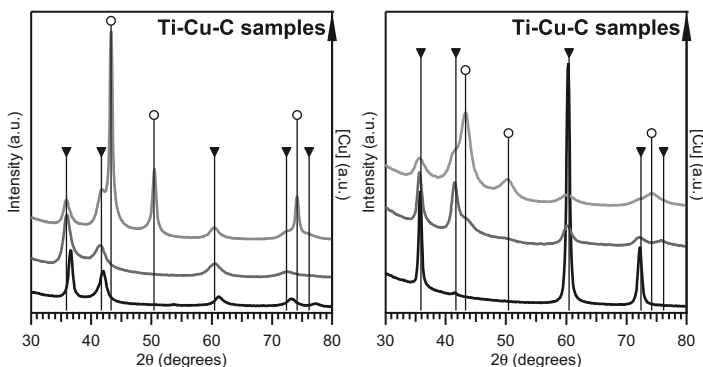


Figure 5.27 XRD of low and medium carbon-content Ti-Cu-C series, see Figure 5.26. Markers show reference positions for TiC (▼) and Cu (○) phases.^{91, 104}

From the XRD, see Figure 5.27, it is clear that the solubility of Cu in TiC indeed is smaller than in above cases. Crystalline Cu is observed in all but one ternary sample. That a solid solution carbide, $(\text{Ti}_{1-x}\text{Cu}_x)\text{C}_y$, is formed in all ternary samples is indicated by similar influence on the carbon-bonding as in the Ti-Ni-C and Ti-Pt-C cases, see Figure 5.28. Additionally, severe sputter damage has been observed for these coatings, also indicating a destabilisation of the carbide phase, see paper I. It is thus concluded that one single phase $(\text{Ti}_{1-x}\text{Cu}_x)\text{C}_y$ sample was synthesised (left, middle in Figure 5.27-27); and that all other samples are nanocomposites consisting of three phases: nc- $(\text{Ti}_{1-x}\text{Cu}_x)\text{C}_y$ / a-C / nc-Cu.

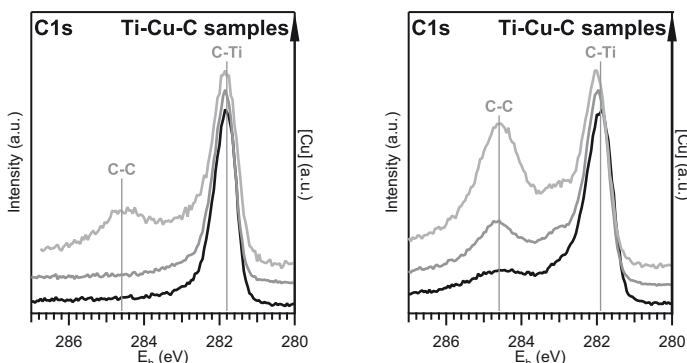


Figure 5.28 XPS the two sample series marked in Figure 5.26. Left the series with ~32 at.% C, and right the series with ~42 at.% C. Spectra obtained after sputter etching to a depth of ~150Å using 200 eV Ar^+ ions. Top spectra in left panel has been shifted due to probable charging during measurement.

As can be seen from Figure 5.27, the lattice parameter of the Cu phase perfectly matches the reference;¹⁰⁴ but for the lattice parameter of the carbide phase no clear trend can be observed. The carbon-rich samples (not shown) exhibit a decrease of lattice parameter as a function of Cu-content. The three-phase microstructure is quite complex: Some solubility of Cu is expected in both carbide and a-C phase, TiC_x has variable stoichiometry, and the lattice parameter of TiC_x nanocrystallites in a-C also varies. Some small shifts are also observed in the $\text{Cu}2p$ and $\text{Ti}2p$ XPS spectra, but also here no clear trends can be observed. Hence the finer details of the samples presently remain undetermined.

It has thus been shown that metastable solid solution carbides $(\text{Ti}_{1-x}\text{Ni}_x)\text{C}_y$ and $(\text{Ti}_{1-x}\text{Cu}_x)\text{C}_y$ can be formed, in agreement with theoretical predictions (see page 50). Additionally it was found that solid solution carbides could be formed in the Ti-Pt-C system. The alloying of TiC with a weak carbide forming metal (e.g. Ni, Pt and Cu) can be seen as a destabilisation of the TiC-phase. In agreement with the simulations, the experimental results also

showed that Cu causes a larger destabilisation than Ni. Pt was found to cause an intermediate destabilisation. The alloying was found to influence microstructure, most notably the amount of a-C phase and grain size, in the as-deposited coatings and decomposition of the metastable supersaturated solid solution carbides gave further design possibilities.

Properties of carbide and nanocomposite coatings

The properties of nanocomposites are largely controlled by their microstructure. In the present work the largest influence has been found from the amount of a-C matrix phase. Samples with a-C content spanning from 0% (pure carbide) to 88% have been studied. The microstructural evolution of these coatings is sketched in Figure 5.29. Here two possible routes are given, one for isotropic (lower part) and one for columnar (top part) growth. In the present work columnar growth has been the general case, see cross section SEM and TEM in Figure 5.4, 5.12 and 5.20 as well as top-view TEM in Figure 5.1. Hence the properties below will be discussed using the upper part of Figure 5.29 as a model.

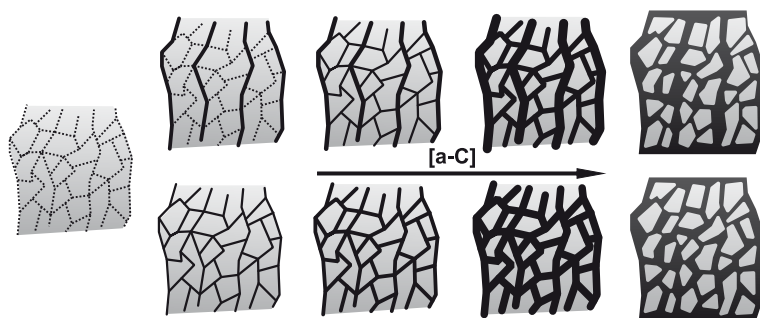


Figure 5.29 Sketch of the microstructural evolution of coatings as the amount of a-C matrix phase increases. Top, non-isotropic route for columnar growth. Bottom, isotropic route for non-columnar growth, favoured by e.g. high substrate bias conditions.

Values for hardness and Young's modulus for nc-TiC_x/a-C nanocomposites found in literature varies quite a lot, see the review by Martínez-Martínez et al.²⁵ and chapter 2. The hardness of the coatings produced in the present study is in the lower range of the literature values, see Figure 5.30 (left, Δ -markers) and papers V and VII. In agreement with literature a slight 'nanocomposite hardening' was observed with about 40% a-C phase.²⁵ The lack of a larger 'nanocomposite hardening' is probably due to the columnar growth, see Figure 5.29. As a-C phase is formed it is accumulated in the column boundaries, and thereafter percolates the columns and surrounds the grains. Before all grains are surrounded by the small amount of matrix / tissue phase

which can give a hardening of the nanocomposite,³² the thickness of a-C in the column boundaries is thick enough to soften the coating. A further possibility is the coatings, due to the low temperature and bias during depositions, are not fully dense, thus preventing high hardness. The Young's modulus was generally found to decrease with increasing amount of a-C phase, see Figure 5.30 (left, ○-markers). The formation of a Ni-containing solid solution carbide leads to a decrease both in hardness and Young's modulus. This is consistent with a weakening of the average Me-C bond in the carbide. Nanoindentation was not performed on Pt- and Cu-containing samples.

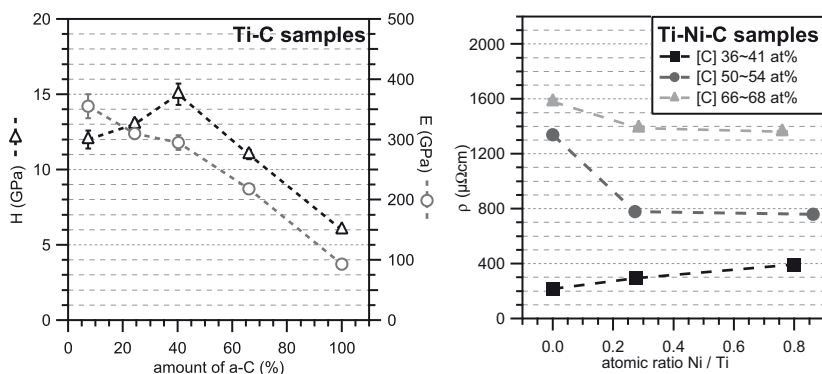


Figure 5.30 Left, Hardness and Young's modulus for a series of Ti-C samples, ranging from almost pure carbide (far left) to pure a-C (far right part). Right, Electrical resistivity measurements at room temperature for Ti-Ni-C samples. Binary samples found on the left side.

The resistivities of binary Ti-C materials were measured in several studies, see papers IV, V and VII. The results are illustrated in Figure 5.30 (right) where Ti-C samples are shown together with Ti-Ni-C samples. Pure TiC_x samples exhibited a resistivity in the range 200 - 400 $\mu\Omega\text{cm}$, which is in agreement with literature. The nc- $\text{TiC}_x/\text{a-C}$ samples show resistivities in the range of 1 000 - 5 000 $\mu\Omega\text{cm}$, which is explained by the low conductivity of the a-C phase for which values in the order of 40 000 $\mu\Omega\text{cm}$ were attained. There is, however, no linear correlation between the amount of a-C phase and the resistivity, showing that the conduction mechanism is more complex than a mixing of two conducting phases.

When TiC_x is alloyed with Ni, forming $(\text{Ti}_{1-x}\text{Ni}_x)\text{C}_y$ the resistivity increases, see Figure 5.30 (right, ■-markers). This can be explained by the decreasing grain size and the introduction of point-defects (Ni-atoms). The nanocomposite samples, on the other hand, exhibit a decrease in resistivity upon introduction of Ni, see Figure 5.30 (right, ◆- and ▲-markers). This is despite an increase in the relative amount of poorly conductive a-C, and a decrease in carbide grain size. The cause of this decrease is presently poorly understood. No resistivity measurements were performed on Ti-Pt-C or Ti-Cu-C samples.

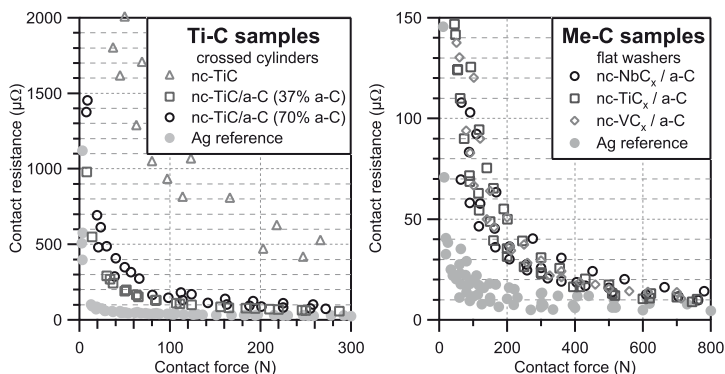


Figure 5.31 Static contact resistance for binary samples measured on two set-ups- Left, Ti-C samples of varying carbon content measured with crossed cylinders. Right, comparable NbC_x/a-C, VC_x/a-C and TiC_x/a-C samples measured with flat washers. Ag vs Ag shown as a reference of an optimal contact resistance.

The static contact resistance was measured in several studies (IV, V and VII), representative data are presented in Figure 5.31. The general observed trend is the opposite to what was found for the resistivity. TiC_x coatings with a low resistivity were found to have a high contact resistance, while the nc-TiC_x/a-C coatings, with distinctly higher resistivity, was found to have low contact resistance. This is shown in Figure 5.31 (left). When an a-C matrix is introduced in the microstructure the contact resistance drops. When the amount of a-C matrix increases the resistance rises. Several series of experiments suggest that a small amount of matrix phase is optimal. The exact amount is probably closely connected to the distribution of matrix phase (c.f. Figure 5.29) and grain size, hence making the optimisation somewhat more complicated. That the behaviour of these nanocomposites is in accordance with a more generic pattern, not specific for the case of TiC_x is shown in Figure 5.31 (right). Here the static contact resistance for nc-NbC_x/a-C, nc-VC_x/a-C and nc-TiC_x/a-C samples is shown. All three coatings exhibit identical performance. The samples were deposited under similar conditions, but unlike the TiC_x-based sample the NbC_x- and VC_x-based samples have not been subjected to any composition optimization. A ZrC_x-based nanocomposite was also measured (not shown), but exhibited a markedly higher contact resistance, most likely due to larger amount of a-C phase (c.f. Figure 5.14).

The low contact resistance for the nanocomposites (with high resistivity) illustrates that the contact resistance is dependent on both electrical and mechanical properties. It also illustrates that a thin coating does not require a very low resistivity to give low contact resistance. The above findings are somewhat strange from the perspective of traditional contact theory (c.f. chapter 3,) which states that the softest material in a mechanical contact deforms. Since all measurements in the present studies were made against a

softer counter contact (Ag), it would be expected to deform and give an equal load-bearing area regardless of the properties of the carbide-based coating. What, however, may explain the observed behaviour is a difference in penetration of the surface oxide film which is present in all cases. It is possible that the nanocomposite samples, on the nanometre scale deform more than the carbide samples. This may cause more frequent penetration of the surface oxide film, and hence giving a larger conductive area and lower constriction and coating resistance.

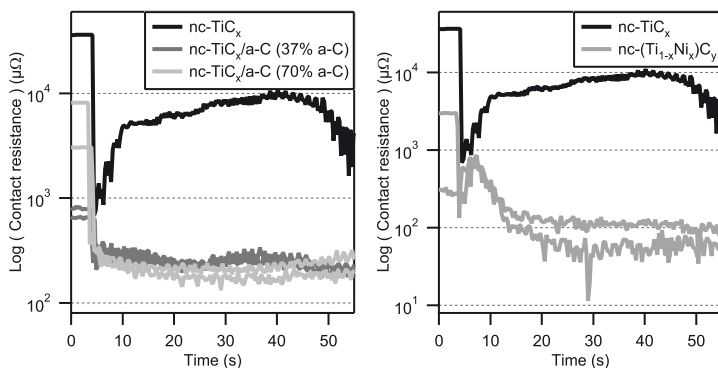


Figure 5.32 Dynamic contact resistance measured in a reciprocating crossed-rod set-up with a contact force of 40 N. Left panel shows same carbide and nanocomposite samples as in Figure 5.31(left). Right panel shows carbide samples: TiC_x and $(\text{Ti}_{1-x}\text{Ni}_x)\text{C}_y$ sample (\diamond -markers in Figure 5.16).

Tests with dynamic contact resistance were also performed, see also paper **VIII**. The coated contact cylinder (c.f. Figure 4.7) was, during measurement of the contact resistance, at a contact force of 40 N given a reciprocating movement. Results from these measurements are presented in Figure 5.32. The left panel once again clearly shows the low contact resistance of nanocomposite $\text{ncTiC}_x/\text{a-C}$ coatings in contrast to the high contact resistance of a nc-TiC_x coating. The right panel shows the same nc-TiC_x and one $\text{nc-(Ti}_{1-x}\text{Ni}_x)\text{C}_y$ coatings (these samples marked \diamond in Figure 5.16). As can be seen there is a drastic difference, the metastable solid solution carbide behaves like the nanocomposites in the left panel. In the as-deposited state both these coatings have been characterised as pure carbide samples with an a-C of less than 4%, and have very similar hardness (15 and 12 GPa) and Young's modulus (277 and 242 GPa). Initial XPS analysis of the wear spot on the coating shows markedly less Ti-O bonds than in unworn surfaces. This suggests that the drop in resistance is connected to a penetration or removal of the surface oxide. Why the Ni-alloyed sample gives a better removal of the surface oxide is not clear, but one possibility is a local decomposition of the underlying carbide grains due to the energy provided in the sliding contact and from resistive heating of the a-spots. Another possibility is that the surface oxide is thinner / less dense before the test

starts, but no distinct differences are observed in surface XPS. Dynamical contact resistance was tested for all polycrystalline and nanocomposite samples shown in Figure 5.16. For all samples except the binary nc-TiC_x sample, the steady-state contact resistance obtained during reciprocal sliding was found to be directly dependent on the coating resistivity. This suggests that the constriction resistances (and conductive area) are identical and that the coating resistance determines this contact resistance. This would also be the case if the surface oxide is completely removed and softer Ag counter determines load-bearing area and conductive area.

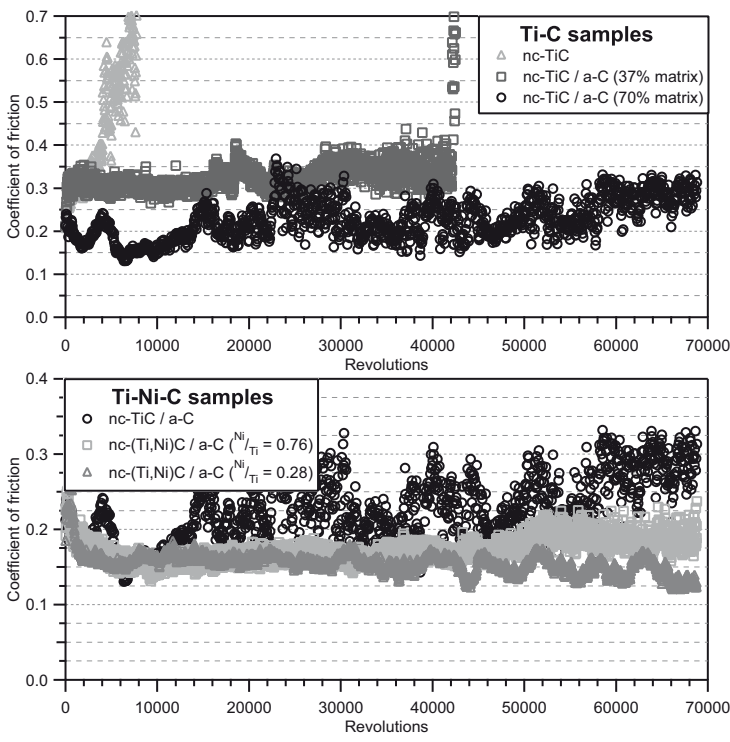


Figure 5.33 Coefficient of friction from ball-on-disc test. Top, for three Ti-C samples of varying composition: one carbide and two nanocomposites. Bottom for three Ti-Ni-C nanocomposite samples with comparable total carbon-content. Note different y-scales in top and bottom graph.

In addition, the tribological properties were studied. Results are illustrated by data from pin-on-disc test in Figure 5.33. In agreement with literature a large influence on the amount of a-C phase was observed,²⁵ see top panel. As can be seen, the pure carbide sample shows a continuously increasing coefficient of friction and fails after roughly 8 000 revolutions. While the two nanocomposite samples (where the a-C phase can act as a solid lubricant) have lower friction and longer lifetime, surviving about 40 000 and 70 000 revolutions, respectively. The results obtained with Ni-alloyed nanocom-

posite samples (marked by a grey area in Figure 5.16) are shown in Figure 5.33(bottom). As can be seen, a lowering of the coefficient of friction is observed. If this is the effect of low-temperature decomposition (2.2) similar to what Wilhelmsson et al. and Lindquist et al. reported,⁵⁵⁻⁵⁷ or an effect on the microstructure can presently not be determined. The attained friction values are comparable to commercial low-friction coatings, and a lifetime of 70 000 revolutions must be considered long. Ti-Cu-C samples (not shown) did not exhibit any reduction in friction at ambient test conditions compared to Ti-C samples, probably due to the presence of Cu-particles.

In summary, it can thus be concluded that carbide-based nanocomposite coatings can be designed to have low contact resistance, low wear and low friction. The contact resistance results suggests that ability of the carbide-based coating to penetrate or remove its (and possibly also the counter surface's) surface oxide is critical for the contact performance. Low contact resistance can be achieved both by ternary carbide and by carbide-based nanocomposite coatings. If low contact resistance and low friction / wear is required for an application, only nanocomposite coatings have the required combination of properties.

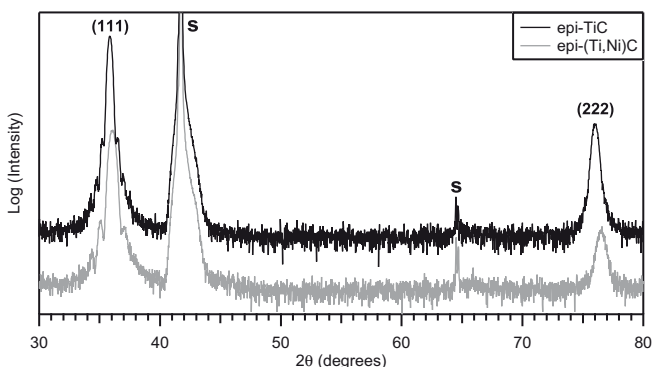


Figure 5.34 Locked couple XRD from carbides deposited on α -Al₂O₃(001) at 400°C. S marks substrate peaks. Notice thickness fringes on carbide (111) diffraction peaks, which indicate a very smooth coating.

Template based graphene synthesis on epitaxial carbide

The last couple years, graphene (i.e. monolayer graphite) has attracted a very large interest due to its unique properties such as being a zero-bandgap semiconductor and possessing extremely large electron mobility.¹⁰⁵⁻¹⁰⁷ Graphene can be synthesised in many ways, among the more common are exfoliation from graphite, epitaxial growth on Ni and MeC-surfaces using, e.g. gaseous carbon source at temperatures of 800-1200°C.¹⁰⁸⁻¹¹¹ Another method of synthesising graphene is the decomposition of single crystal SiC, which is carried out at 1400°C.¹¹² Our results show that alloying TiC_x with a weakly carbide forming metal (such as Ni) will promote the formation of a carbon phase at the surface during annealing. It is hence plausible that graphene synthesis could be achieved at lower temperatures than previously reported. To test this, epitaxially grown supersaturated solid solution carbide samples are required.

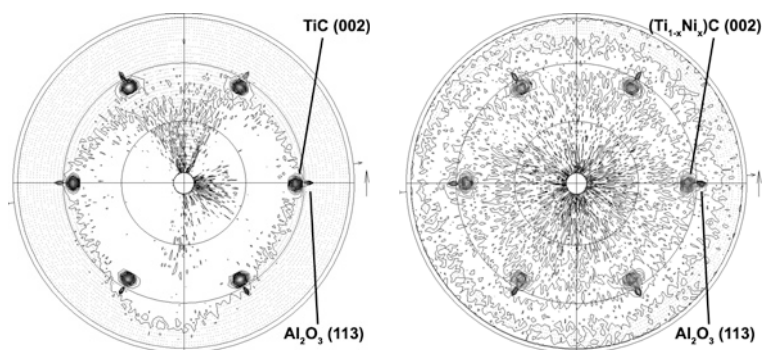


Figure 5.35 TiC(002) pole figures of the epi-TiC (left) and epi-(Ti,Ni)C samples. In the pole figure $\alpha\text{-Al}_2\text{O}_3(113)$ also shows as small but distinct peaks. Both substrate and coating show twinning, and hence a 6-fold symmetry.

Epitaxial metal carbide coatings can easily be deposited by magnetron sputtering providing that suitable substrate material is used. In this thesis epitaxial coatings of both Ti-C and Ti-Ni-C were deposited on single crystalline $\alpha\text{-Al}_2\text{O}_3(001)$ substrates at 400°C. Locked-couple XRD and pole-figures are shown in Figure 5.34 and Figure 5.35, respectively. From these data, and additional XRD and XPS measurements, the crystallographic relations and compositions were determined. Results are summarised in Table 5.3. As can be seen, the lattice parameter of the ternary sample is smaller than the lattice parameter of the binary sample; both in- and out-of-plane with the substrate, indicating that Ni is in solid solution. The coherence lengths determined from Scherrer's equation suggest that the material consist of grains growing undisturbed through the entire thickness of the coating; and that the domains have an aspect ratio of about 3. All these analysis were made after samples were removed from the vacuum system where they were synthesised.

Table 5.3 Summary of XRD results. a_{\perp} and a_{\parallel} are lattice parameter determined from TiC(111) and TiC(220), respectively. t_{\perp} and t_{\parallel} are coherence length determined by Scherer's equation from TiC(111) and TiC(220), respectively. \perp and \parallel indicate directions orthogonal or parallel to the substrate surface. d is the sample thickness determined by XRR.

Carbide stoichiometry	a_{\perp} (Å)	a_{\parallel} (Å)	t_{\parallel} (nm)	t_{\perp} (nm)	d (nm)	orientation
TiC _{0.82}	4.355	4.345	20	7	24	α -Al ₂ O ₃ (001)[110] // TiC(111)[10-1]
(Ti _{0.86} Ni _{0.14})C _{0.80}	4.330	4.335	13	5	14	α -Al ₂ O ₃ (001)[110] // (Ti,Ni)C(111)[10-1]

To investigate the possibility to form graphene through decomposition of the solid solution carbide, annealing experiments have been conducted.¹¹³ Unfortunately surface analysis equipment was not available in the synthesis chamber, nor was inert transfer possible. Coatings were hence first exposed to air, and thereafter introduced to a second vacuum system where cleaning, annealing and in-situ characterisation took place. Surface cleaning was carried out by cycles of Ar⁺ (500-1000 eV) etching and continuously increased heating. At annealing temperatures of 700°C segregation of carbon on the surface can be observed through XPS. From 800°C the obtained LEED-pattern sharpens, see Figure 5.36 (left). Two, to each other rotated, hexagonal patterns can be identified. This observation is in agreement with references,^{109, 110} and is hence consistent with monolayer graphite and a TiC-based carbide. Due to that the lattice parameter of Ni and Graphene coincide, and since Ni-segregation was observed for nanocomposite samples from 600°C it can presently not be excluded that Ni also is contributing to the observed LEED-pattern.

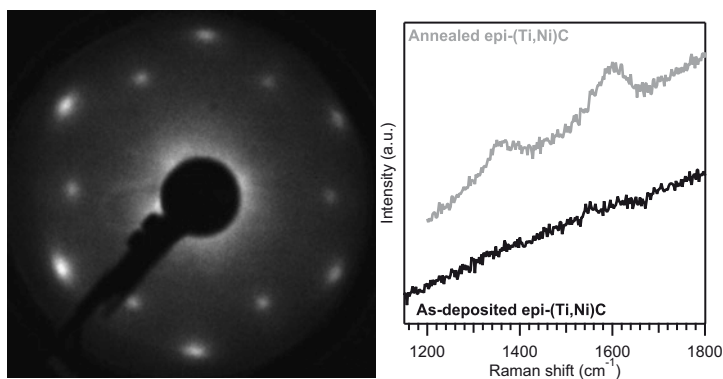


Figure 5.36 Left, LEED-pattern from the cleaned and annealed epi-(Ti_{0.86}Ni_{0.14})C_{0.80} sample. Right, Raman spectra of as-deposited (black) and annealed (grey) epi-(Ti_{0.86}Ni_{0.14})C_{0.80} sample.

Raman spectra (obtained ex-situ) from a sample exhibiting such a LEED-pattern, and an as-deposited reference, are shown in Figure 5.36 (right). Weak D- and G- peaks are visible for the annealed, but not for the as-deposited sample. This shows that carbon is present at the surface, but it also shows that the carbon is not perfectly ordered. The D-peak is generally not present in perfect graphene sheets. Continued annealing leads to growth of the outer LEED-spots (from carbon) and the formation of a ring. This is interpreted as continued carbon segregation and increasing disorder, in particular in-plane rotations.

It is thus likely that ordered, very thin, layers of carbon have been formed by decomposition of epitaxial supersaturated solid solution carbide coatings. This has been achieved at lower temperatures than other similar synthesis techniques. If the obtained carbon layers can be classified as graphene sheets, and if they are transferable to other substrates remain to be determined. Studies to determine this will continue, and will be published in due course.¹¹³

6. Concluding remarks

The subject of the present thesis is synthesis, microstructure and properties of carbide-based nanocomposites. Thin film nanocomposites have been synthesised by dc magnetron sputtering and characterised with regard to composition and, microstructure as well as mechanical and electrical properties. The main analysis techniques have been X-ray photoelectron spectroscopy and X-ray diffraction.

It has been shown that nc-MeC_x/a-C (Me = Ti, Nb or V) nanocomposite coatings give a low contact resistance in electrical contacts when mated against Ag. Lowest contact resistance is attained by coatings with a small amount of a-C. Furthermore these nanocomposite coatings have superior tribological properties (low wear and friction) compared to traditional noble metal coatings used in electrical contacts. This makes them an attractive choice for sliding contact arrangements or such applications where the contact is frequently connected and disconnected. Results suggest that the contact resistance against a Ag counter contact of these nanocomposite coatings primarily is determined by their ability to penetrate the surface oxide. Up-scaling studies were also undertaken, and show that laboratory performance can be reproduced in a semi-industrial scale. This indicates that production of the material is possible also on an industrial scale.

In the studies of nc-TiC_x/a-C nanocomposites it has been shown that a distinctly different bonding state exists at the interface between the two phases. This includes considerable charge-transfer from Ti3d to C2p states over the interface. This charge-transfer is connected to a, with reduced grain sizes, increasing lattice parameter of TiC_x. This model is supported by results from XPS, SXE / SXA and theoretical simulations using DFT.

Further design possibilities of the TiC_x-based nanocomposites have been demonstrated by alloying with weakly carbide forming metals (i.e. Me = Ni, Cu or Pt). Upon alloying, metastable supersaturated solid solution carbides, (Ti_{1-x}Me_x)C_y, are formed. This destabilisation of the TiC_x-phase leads to changes in the phase distribution in the as-deposited nanocomposites, thus giving further control over the amount of carbon phase. Additional design possibilities also become available through the possible decomposition of the metastable (Ti_{1-x}Me_x)C_y. Different annealing conditions will yield either more a-C phase, or a new metallic Me-phase. This alloying concept was also

investigated theoretically for all 3d transition metals using theoretical simulations and DFT.

It has also been demonstrated that Ar^+ ion etching, which is commonly used during analysis of carbide based nanocomposites, can severely distort the result of the analysis, especially for materials containing metastable phases. This implies that special methods or considerable care must be taken during analysis, and that much of the previously published results may contain errors. Analysis schemes to detect and minimize the effect of this have been developed.

7. Acknowledgements

Mitt första tack vill jag rikta till min handledare professor Ulf Jansson, för inspirerande, tålmodigt och uppmuntrande handledning, samt för att han gett mig möjligheten att forska på spännande kolbaserade material. Ola, som introducerade mig för allt praktiskt, och mycket teoretiskt, när det gäller vakuum, tunnfilmer och sputtring, ett stort tack för det och alla övriga frågor vi diskuterat genom åren!

Tack till alla mina kollegor på institutionen för materialkemi, för att ha gjort det roligt att åka till Ångström även på morgnar då forskningen gått trögt. Särskilt tack till Erik för sällskap på kontoret dagar, kvällar och helger samt många diskussioner om allt och inget. Stort tack även till Erika, Tanguy, Martin, David, Anna, Wendy och Oscar för många trevliga stunder utanför Ångström och forskningen. Ett extra tack Erik och Eva för goda råd i skidbacken ("börja med att sätta skidorna på samma sida björken") och för att ha dragit ut mig i mer snö än jag trodde jag skulle ta mig fram genom levande. Ser fram emot att kunna åka skidor med er fler vintrar! Även Mats Boman förtjänar ett hedersomnämmande för goda mat och dryckesdiskussioner, liksom Anders Eriksson för en ha gett bra start på min kemistutbildning genom att med fast hand och god pedagogik styra och undervisa på kemi grundkurs HT99. Tack till Matilda och Nils som gör att jag kan lämna Svanslös i goda händer. Fortsätt som ni börjat, med nyfikna frågor och ivrigt forskande, så kommer det gå bra för er! (Gäller även Mattis) Även tack till Simon, Erik T, Andreas och Tina det var ett nöje att arbeta med er under era exjobb.

Stora tack till Anders och Janne, utan vars slit i verkstan min forskning bokstavligen aldrig kommit längre än till ritbordet. Det har varit kul och givande att arbeta med er! Tack även till Ottosson för ett välfungerande röntgenlab. Eva, Gunilla och Tatti, utan er hade jag väl aldrig ens kommit in i huset! Tack för att ha hållt ordning på mig och hjälpt mig med allt från tågbiljetter till inläsning av platinabitlar.

Mattias, Benny och Urban tack för att ha introducerat mig till, och guidat mig i tribologins värld. Och tack Åsa för diskussioner och funderingar kring elektriska kontakter. Tack till Impact Coatings och ABB och där inblandade personer, särskilt Åke Öberg, för att ha gett mig ett tillämpningsområde som gör att jag kan förklara min forskning för lekmän. Tack till Svante, Ela, Hans och Anders S för att ha introducerat mig för synkrotronstrålar och HIKE-

metoden. An especialy large thanks to Ela, for generously giving me access to her beamtime and helping me with measurements. Tack till Micke för att hjälpa mig att utvidga mina idéer med hjälp av teoretiska beräkningar och för givande diskussioner. Tack till Sigita för hjälp med TEM och tålmodigt förklarande vid mikroskopet, till Göran Possnert för hjälp med ERDA-mätningar, och till Pål för slit med att försöka få mina karbider att göra grafen. Ich möchte mich ferner auch beim Herrn Dr. Michael Stüber und den anderen Mitarbeitern des IMF I, Forschungszentrums Karlsruhe für interessante und fruchtbare Zusammenarbeit bedanken. Frida, in den Diskussionen mit Dir war es besonderes toll zu entdecken, dass ich tatsächlich über Forschung auf Deutsch diskutieren kann, danke! Einen Gedanken auch zu Martina, für hilfe mit TEM. Tack till alla vid tunnfilmgruppen (och andra relevanta grupperingar) vid LiU för samarbete och trevligt umgänge vid diverse möten och konferenser. Särskilt tack till Stina, Per P, Jun Lu, Martin M och Per E.

Tack till Teknophonorkestern Tupplurarna och dess musiker för att under min tid som student i Uppsala, ha gett mig mycket glädje, och inte minst värdefulla vänner. Även de vänner som inte passar in ovan, särskilt Sven och Linus, som inte glömmer bort mig bara för att jag grottar ner mig i min forskning och gömmer mig på Ångström förtjänar ett tack.

Och slutligen, ett stort tack till min familj för stöd och uppmuntran, särskilt Mamma och Pappa, som även gett mig en kul blandning av ingenjörssinne och klassisk akademisk bildning.

8. References

1. **Vopiscus, F.**, *Scriptores Historiae Augustae: Firmus Saturninus Proculus et Bonosus, VIII, 10*, (Loeb classical library, English translation by David Magie, Heinemann, London, 1921), 4th century A.D.
2. Freestone, I., et al., *The Lycurgus Cup - A Roman nanotechnology*, **Gold Bulletin** 40 (2007), p. 270
3. Hunt, L.B., *The true story of purple of Cassius*, **Gold Bulletin** 9 (1976), p. 134
4. Berzelius, J.J., *Försök - till ett rättfärdigande af de theoretiskchemiska åsikter, på hvilka den systematiska uppställningen i mitt Försök till en förbättring av den chemiska nomenclaturen grundar sig.*, **Kongl. vetenskaps academiens handlingar** (1813), p. 175
5. Berzelius, J.J., *Ueber den Cassius'chen Goldpurpur*, **Annalen der Physik und Chemie** (1831), p. 306
6. Faraday, M., *Experimental relations of Gold (and other metals) to light*, **Philosophical transactions of the Royal Society** 147 (1857), p. 145
7. Mie, G., *Beiträge zur Optik trüber Medien, speziell kolloidaler Metallösungen*, **Annalen Der Physik** 25 (1908), p. 377
8. Kelly, K.L., et al., *The optical properties of metal nanoparticles: The influence of size, shape, and dielectric environment*, **Journal of Physical Chemistry B** 107 (2003), p. 668
9. Larsson, S. and Ek, E., *Elavbrottet 23 september 2003 - händelser och åtgärder*. 2003, Svenska kraftnät
10. **Hägg, G.**, *Allmän och oorganisk kemi*, Almqvist & Wiksell, Uppsala, 1963.
11. **Shriver, D.F. and Atkins, P.W.**, *Inorganic Chemistry*, Third ed., Oxford University Press, Oxford, 1999.
12. Ettmayer, P. and Lengauer, W., *Carbides: Transition Metal Solid State Chemistry*, in **Encyclopedia of Inorganic Chemistry**, (R.B. King, ed.), John Wiley & Sons Ltd., Chichester, 1994.
13. Meschel, S.V. and Kleppa, O.J., *Standard enthalpies of formation of some 3d transition metal carbides by high temperature reaction calorimetry*, **Journal of Alloys and Compounds** 257 (1997), p. 227
14. Ono, S., Kikegawa, T., and Ohishi, Y., *A high-pressure and high-temperature synthesis of platinum carbide*, **Solid State Communications** 133 (2005), p. 55
15. Häglund, J., et al., *Theory of bonding in transition-metal carbides and nitrides*, **Physical Review B** 48 (1993), p. 11685 LP
16. Häglund, J., et al., *Band structure and cohesive properties of 3d-transition-metal carbides and nitrides with the NaCl-type structure*, **Physical Review B** 43 (1991), p. 14400 LP
17. Zhang, Y.F., et al., *A theoretical study on the chemical bonding of 3d-transition-metal carbides*, **Solid State Communications** 121 (2002), p. 411
18. Williams, W.S., *Electrical properties of hard materials*, **International Journal of Refractory Metals & Hard Materials** 17 (1999), p. 21

19. Robertson, J., *Diamond-like amorphous carbon*, **Materials Science and Engineering R** 37 (2002), p. 129
20. Massalski, T.B., *Binary Alloy Phase Diagrams*, Vol. 1, American Society for Metals, Metals Park, 1986.
21. Voevodin, A.A. and Zabinski, J.S., *Load-adaptive crystalline-amorphous nanocomposites*, **Journal of Materials Science** 33 (1998), p. 319
22. Feng, B., et al., *Characterization of microstructure and mechanical behavior of sputter deposited Ti-containing amorphous carbon coatings*, **Surface and Coatings Technology** 148 (2001), p. 153
23. Stüber, M., et al., *Microstructure and properties of low friction TiC-C nanocomposite coatings deposited by magnetron sputtering*, **Surface and Coatings Technology** 150 (2002), p. 218
24. Pei, Y.T., et al., *Nanostructured TiC/a-C coatings for low friction and wear resistant applications*, **Surface and Coatings Technology** 198 (2005), p. 44
25. Martínez-Martínez, D., et al., *Influence of the microstructure on the mechanical and tribological behavior of TiC/a-C nanocomposite coatings*, **Thin Solid Films** 517 (2009), p. 1662
26. Gulbinski, W., et al., *Evaluation of phase, composition, microstructure and properties in TiC/a-C:H thin films deposited by magnetron sputtering*, **Applied Surface Science** 239 (2005), p. 302
27. Delplancke-Ogletree, M.-P. and Monteiro, O.R., *Deposition of titanium carbide films from mixed carbon and titanium plasma streams*, **Journal of Vacuum Science & Technology A** 15 (1997), p. 1943
28. Zehnder, T. and Patscheider, J., *Nanocomposite TiC/a-C:H hard coatings deposited by reactive PVD*, **Surface and Coatings Technology** 133-134 (2000), p. 138
29. Grischke, M., *Entwicklung eines Strukturmodells metallhaltiger Kohlenwasserstoff-Schichten [a-C:H(Me)] mit carbidbildender Metallkomponente*, VDI Fortschrittberichte, Reihe 5, Nr 179, VDI verlag, Düsseldorf, 1989.
30. Wänstrand, O., Larsson, M., and Hedenqvist, P., *Mechanical and tribological evaluation of PVD WC/C coatings*, **Surface and Coatings Technology** 111 (1999), p. 247
31. Nilsson, D., et al., *Low-friction carbon-rich carbide coatings deposited by co-sputtering*, **Wear** 254 (2003), p. 1084
32. Zehnder, T., et al., *Nanostructural and mechanical properties of nanocomposite nc-TiC/a-C:H films deposited by reactive unbalanced magnetron sputtering*, **Journal of Applied Physics** 95 (2004), p. 4327
33. Benndorf, C., et al., *Electrical conductivity and microstructure of metal containing a-C:H films*, **Synthetic Metals** 43 (1991), p. 4055
34. Huang, Q.F., et al., *Molybdenum-containing carbon films deposited using the screen grid technique in an electron cyclotron resonance chemical vapor deposition system*, **Diamond and Related Materials** 9 (2000), p. 534
35. Huang, Q.F., et al., *Conduction mechanism in molybdenum-containing diamond-like carbon deposited using electron cyclotron resonance chemical vapor deposition*, **Journal of Applied Physics** 88 (2000), p. 4191
36. Sedláčková, K., et al., *C-Ti nanocomposite thin films: Structure, mechanical and electrical properties*, **Vacuum** 82 (2008), p. 214

37. Trindade, B., Cavaleiro, A., and Vieira, M.T., *The influence of the addition of a third element on the structure and mechanical properties of transition-metal-based nanostructured hard films: Part II - Carbides*, in **Nanostructured Coatings**, (A. Cavaleiro and J.T.M. De Hosson, eds.), Springer Science+Business Media, New York, 2006.
38. Patscheider, J. and Haug, F.-J., *Understanding nanostructured hard coatings – the importance of interfaces and interphases*, **International Journal of Materials Research** (2005), p. 493
39. Schier, V., Michel, H.-J., and Halbritter, J., *ARXPS-analysis of sputtered TiC, SiC and Ti_{0.5}Si_{0.5}C layers*, **Fresenius' Journal of Analytical Chemistry** 346 (1993), p. 227
40. Hornetz, B., Michel, H.-J., and Halbritter, J., *ARXPS-analysis and morphology of sputtered nanocrystalline TiC/SiC coatings*, **Fresenius' Journal of Analytical Chemistry** 349 (1994), p. 233
41. Mani, A., et al., *Effects of residual stress on the mechanical and structural properties of TiC thin films grown by RF sputtering*, **Surface and Coatings Technology** 194 (2005), p. 190
42. Li, G. and Xia, L.F., *Structural characterization of TiC_x films prepared by plasma based ion implantation*, **Thin Solid Films** 396 (2001), p. 16
43. Kuznetsov, M., et al., *Investigation of TiC-C coatings by X-ray photoelectron spectroscopy*, **Journal of Surface Investigation: X-ray, Synchrotron and Neutron Techniques** 3 (2009), p. 331
44. Luthin, J., et al., *Ion beam-induced carbide formation at the the titanium-carbon interface*, **Nuclear Instruments and Methods in Physics Research Section B** 182 (2001), p. 218
45. Ernst, K.-H. and Oral, B., *On the chemistry at the Si,Ti-doped a-C:H/TiC interface*, **Thin Solid Films** 446 (2004), p. 72
46. Cavaleiro, A., Trindade, B., and Vieira, M.T., *The influence of the addition of a third element on the structure and mechanical properties of transition-metal-based nanostructured hard films: Part I - Nitrides*, in **Nanostructured Coatings**, (A. Cavaleiro and J.T.M. De Hosson, eds.), Springer Science + Business Media, New York, 2006.
47. Bandyopadhyay, D., Sharma, R., and Chakraborti, N., *The Ti- Ni- C System*, **Journal of Phase Equilibria and Diffusion** 21 (2000), p. 186
48. Villars, P., Prince, A., and Okamoto, H., eds., **Handbook of ternary alloy phase diagrams**, Vol. 6, ASM International, London, 1995.
49. Trindade, B. and Vieira, M.T., *Modification of the structural order of transition metal-carbon systems by the addition of a Group VIII element*, **Materials Science and Engineering A** 352 (2003), p. 195
50. Wilhelmsson, O., et al., *Deposition and characterization of ternary thin films within the Ti-Al-C system by DC magnetron sputtering*, **Journal of Crystal Growth** 291 (2006), p. 290
51. Tomé, G., Trindade, B., and Vieira, M.T., *Synthesis and characterisation of new sputtered metastable carbides*, **Vacuum** 64 (2002), p. 205
52. Wilhelmsson, O., et al., *Deposition and characterization of magnetic Ti-Fe-C nanocomposite thin films*, **Thin Solid Films** In Press, Corrected Proof (2009), p. DOI: 10.1016/j.tsf.2009.07.195
53. Turnbull, D., *Metastable structures in metallurgy*, **Metallurgical and Materials Transactions A** 12 (1981), p. 695
54. **Callister, W.D.J.**, *Materials Science and Engineering - An Introduction*, 5th ed., John Wiley & Sons, Inc., New York, 2000.

55. Wilhelmsson, O., et al., *Design of nanocomposite low-friction coatings*, **Advanced Functional Materials** 17 (2007), p. 1611
56. Lindquist, M., et al., *Tribofilm formation and tribological properties of TiC and nanocomposite TiAlC coatings*, **Wear** 266 (2009), p. 379
57. Lindquist, M., et al., *Tribofilm formation from TiC and nanocomposite TiAlC coatings, studied with focused ion beam and transmission electron microscopy*, **Wear** 266 (2009), p. 988
58. Eklund, P., et al., *Microstructure and electrical properties of Ti-Si-C-Ag nanocomposite thin films*, **Surface and Coatings Technology** 201 (2007), p. 6465
59. Endrino, J.L., Nainaparampil, J.J., and Krzanowski, J.E., *Microstructure and vacuum tribology of TiC-Ag composite coatings deposited by magnetron sputtering-pulsed laser deposition*, **Surface and Coatings Technology** 157 (2002), p. 95
60. Bijelovic, S., et al., *A novel wear-resistant magnetic thin film material based on a $Ti_{1-x}Fe_xC_{1-y}$ nanocomposite alloy*, **Physical Review B** submitted (2009)
61. Hugosson, H.W., et al., *Surface segregation of transition metal impurities on the TiC(1 0 0) surface*, **Surface Science** 585 (2005), p. 101
62. **Holm, R.**, *Electrical Contacts - Theory and Applications*, Reprint of the forth completely rewritten ed., 1967, 3rd printing, Springer-Verlag, Berlin, 2000.
63. **Rieder, W.**, *Electrical Contacts - An introduction to their physics and applications*, (G.J. Witter), IEEE, Piscataway, USA, 2005.
64. Slade, P.G., ed. **Electrical contacts - principles and applications**, Marcel Dekker, Inc., New York, 1999.
65. Greenwood, J.A., *Constriction Resistance and Real Area of Contact*, **British Journal of Applied Physics** 17 (1966), p. 1621
66. Groves, W.R., *On the Electro-Chemical Polarity of Gases*, **Philosophical transactions of the Royal Society** (1852), p. 87
67. Thornton, J.A. and Greene, J.E., *Sputter Deposition Processes*, in **Handbook of deposition technologies for films and coatings**, (R.F. Bunshah, ed.), Noyes Publications, Park Ridge, 1994.
68. Parsons, R., *Sputter Deposition Processes*, in **Thin film processes II**, (J.L. Vossen and W. Kern, eds.), Academic Press Inc., San Diego, 1991.
69. Siegbahn, K., *Electron spectroscopy for atoms, molecules and condensed matter*, in **Nobel Lectures, Physics 1981-1990**, (T. Frängsmyr, ed.), World Scientific Publishing Co., Singapore, 1993.
70. **Hüfner, S.**, *Photoelectron spectroscopy*, Third ed., Springer-Verlag, Berlin, 2003.
71. Oswald, S. and Reiche, R., *Binding state information from XPS depth profiling: capabilities and limits*, **Applied Surface Science** 179 (2001), p. 307
72. **Moulder, J., et al.**, *Handbook of X-ray Photoelectron Spectroscopy*, (J. Chastain and R.C.J. King), Physical Electronics, Inc., Eden Prairie, USA, 1995.
73. Ramqvist, L., et al., *Charge transfer in transition metal carbides and related compounds studied by ESCA*, **Journal of Physics and Chemistry of Solids** 30 (1969), p. 1835
74. Didziulis, S.V., et al., *Photoelectron Spectroscopic Studies of the Electronic-Structure and Bonding in Tic and Tin*, **Inorganic Chemistry** 33 (1994), p. 1979

75. Sinharoy, S. and Levenson, L.L., *The formation and decomposition of nickel carbide in evaporated nickel films on graphite*, **Thin Solid Films** 53 (1978), p. 31
76. Ujvári, T., et al., *Composition, structure and mechanical property analysis of DC sputtered C-Ni and CN_x-Ni nano-composite layers*, **Surface and Interface Analysis** 36 (2004), p. 760
77. Zdansky, E.O.F., Nilsson, A., and Mårtensson, N., *CO-induced reversible surface to bulk transformation of carbidic carbon on Ni(100)*, **Surface Science** 310 (1994), p. L583
78. Hamrin, K., et al., *Valence Bands and Core Levels of the Isoelectronic Series LiF, BeO, BN, and Graphite Studied by ESCA*, **Physica Scripta** (1970), p. 277
79. Chu, P.K. and Li, L., *Characterization of amorphous and nanocrystalline carbon films*, **Materials Chemistry and Physics** 96 (2006), p. 253
80. Drube, W., et al., *Tunable high-energy X-ray photoemission*, **Journal of Electron Spectroscopy and Related Phenomena** 88 (1998), p. 683
81. Schäfers, F., Mertin, M., and Gorgoi, M., *KMC-1: A high resolution and high flux soft x-ray beamline at BESSY*, **Review of Scientific Instruments** 78 (2007), p. 123102
82. Gorgoi, M., et al., *The high kinetic energy photoelectron spectroscopy facility at BESSY progress and first results*, **Nuclear Instruments and Methods in Physics Research Section A** 601 (2009), p. 48
83. Birkholz, M., *Thin film analysis by X-ray scattering*, Wiley-VCH Verlag GmbH, Weinheim, 2006.
84. Scardi, P., Leoni, M., and Delhez, R., *Line broadening analysis using integral breadth methods: a critical review*, **Journal of Applied Crystallography** 37 (2004), p. 381
85. Ferrari, A.C., *Raman spectroscopy of amorphous carbon films: State of the art*, **New Diamond and Frontier Carbon Technology** 14 (2004), p. 87
86. Smits, F.M., *Measurement of Sheet Resistivities with the 4-Point Probe*, **Bell System Technical Journal** 37 (1958), p. 711
87. Valdes, L.B., *Resistivity Measurements on Germanium for Transistors*, **Proceedings of the Institute of Radio Engineers** 42 (1954), p. 420
88. Oliver, W.C. and Pharr, G.M., *An Improved Technique for Determining Hardness and Elastic-Modulus Using Load and Displacement Sensing Indentation Experiments*, **Journal of Materials Research** 7 (1992), p. 1564
89. Kohn, W., *Electronic structure of matter - wave functions and density functionals*, in **Nobel Lectures, Chemistry 1986-2000**, (I. Grenthe, ed.), World Scientific Publishing Co., Singapore, 2003.
90. Leach, A., *Molecular Modelling - principles and applications*, Second ed., Pearson Education Limited, Essex, 2001.
91. Morris, M.C., et al., **National bureau of standards (U.S.) monograph 25** section 18 (1981), p. 73
92. Murray, J.L., ed. **Phase Diagrams of Binary Titanium Alloys**, ASM International, Metal Parks, 1989.
93. Fukuhara, M., *Lattice expansion of nanoscale compound particles*, **Physics Letters A** 313 (2003), p. 427
94. Räsander, M. and Lewin, E., *To be published*, (2009)
95. Eklund, P., et al., *Magnetron sputtering of Ti₃SiC₂ thin films from a compound target*, **Journal of Vacuum Science & Technology A** 25 (2007), p. 1381
96. Morris, M.C., et al., **National bureau of standards (U.S.) monograph 25** section 21 (1985), p. 135

97. Will, G. and Platzbecker, R., *Crystal structure and electron density distribution in niobium carbide*, **Zeitschrift Fur Anorganische Und Allgemeine Chemie** 627 (2001), p. 2207
98. Nowotny, H. and Kieffer, R., **Metallforschung** 2 (1947), p. 257
99. Swanson, H.E. and Tatge, E., **National bureau of standards (U.S.) Circular 539** vol. 1 (1953)
100. Nesbitt, H.W., Legrand, D., and Bancroft, G.M., *Interpretation of Ni2p XPS spectra of Ni conductors and Ni insulators*, **Physics and Chemistry of Minerals** 27 (2000), p. 357
101. Song, B., et al., *Valence band structures of titanium nitride and titanium carbide calculated with chemically complete clusters*, **Journal of Physics-Condensed Matter** 10 (1998), p. 9443
102. Swanson, H.E. and Tatge, E., **National bureau of standards (U.S.) Circular 539** vol. 1 (1953), p. 31
103. **Hugosson, H.W.**, Doctoral thesis: *A Theoretical Treatise on the Electronic Structure of Designer Hard Materials*, Department of Physics, Uppsala universitet, 2001. <http://urn.kb.se/resolve?urn=urn:nbn:se:uu:diva-651>
104. Swanson, H.E. and Tatge, E., **National bureau of standards (U.S.) Circular 539** vol. 1 (1953), p. 359
105. Geim, A.K. and Novoselov, K.S., *The rise of graphene*, 6 (2007), p. 183
106. Novoselov, K.S., et al., *Electric Field Effect in Atomically Thin Carbon Films* 10.1126/science.1102896, **Science** 306 (2004), p. 666
107. Katsnelson, M.I., *Graphene: carbon in two dimensions*, **Materials Today** 10, p. 20
108. Aizawa, T., et al., *Anomalous bond of monolayer graphite on transition-metal carbide surfaces*, **Physical Review Letters** 64 (1990), p. 768 LP
109. Itoh, H., et al., *Scanning tunneling microscopy of monolayer graphite epitaxially grown on a TiC(111) surface*, **Surface Science Letters** 254 (1991), p. L437
110. Nagashima, A., et al., *Electronic states of monolayer graphite formed on TiC(111) surface*, **Surface Science** 291 (1993), p. 93
111. Itchkawitz, B.S., et al., *Monolayer graphite on TaC(111): electronic band structure*, **Surface Science** 318 (1994), p. 395
112. Forbeaux, I., Themlin, J.-M., and Debever, J.-M., *Heteroepitaxial graphite on 6H-SiC(0001): Interface formation through conduction-band electronic structure*, **Physical Review B** 58 (1998), p. 16396 LP
113. Palmgren, P., et al., to be published

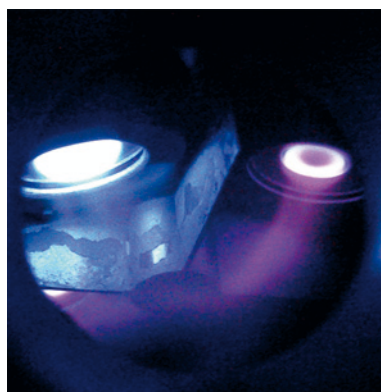
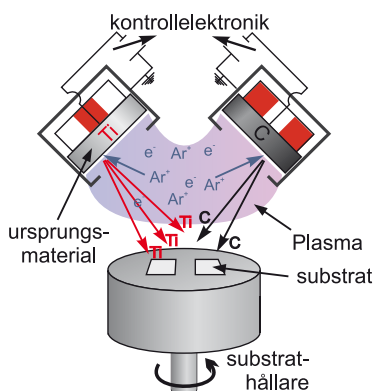
9. Sammanfattning på svenska

Att ge en komponent en ytbeläggning är ett mycket effektivt sätt att höja dess prestanda. Den enklaste formen av ytbehandling är färg, som både ger en vacker yta och skydd mot väder och vind åt en komponent som kanske har en ful yta och är korrosionskänslig, men i gengäld ger en mekanisk stabilitet (tex en cykelram). Materialen som behandlas i denna avhandling utgörs av sk nanokompositerna som har tillverkas i form av ytbeläggningar.

Denna avhandling beskriver studier av material baserade på metallkarbider, en grupp av föreningar bestående av grundämnet kol och ett metalliskt grundämne från de sk övergångselementen. Metallkarbider är generellt hårda, elektriskt ledande och har hög smältpunkt. I detta arbete har metallkarbid kombinerats med amorft kol i en komposit. Kompositen består av små kristaller, 2-50 nm (1 atom $\sim 0,15$ nm, 1 nm = 1/1000 000 000 m), av metallkarbid inbäddade i en sk matris av amorft kol. På grund av de små dimensionerna benämns denna typ av komposit oftast nanokomposit, och skrivs nc-MeC_x/a-C. Egenskaperna av denna komposit är starkt beroende av blandningen av de två ingående faserna, deras relativa mängder, dimensioner och fördelning i materialet. Genom att styra syntesen av dessa material kan specifika blandningar (mikrostrukturer) erhållas och därmed kan nanokompositens egenskaper styras. De små dimensionerna i nanokompositerna, som är i samma storleksordning som många fysiska fenomen, leder till att man med denna typ av material kan kombinera egenskaper som inte tidigare gått att uppnå i ett och samma material.

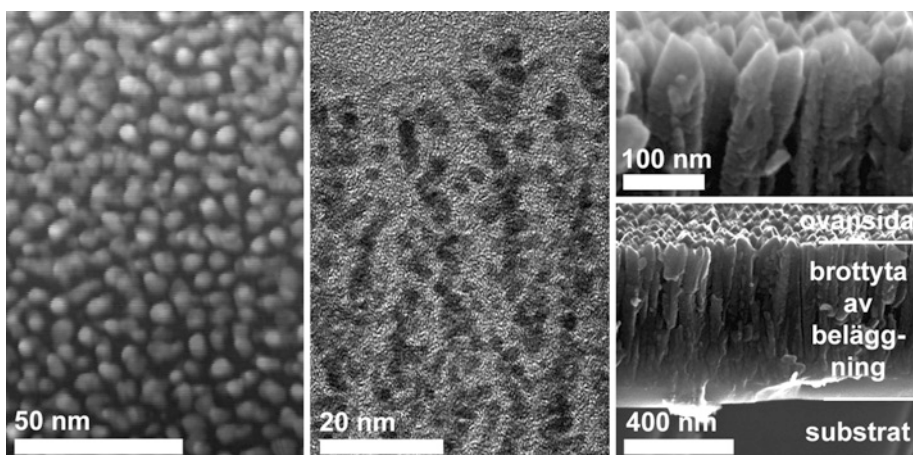
Ett område där ytbeläggningar används är elektriska kontakter. Dessa är ofta belagda med ädla metaller, såsom guld. En guldbeläggning korroderar inte, och eftersom den är mjuk deformeras den när kontaktdonen trycks ihop och ger en stor, metalliskt ledande, yta som kan leda ström med små förluster. Dessa metallbeläggningars mjukhet gör också att de smetas ut och nöts bort tämligen enkelt. Detta ger alltså en kortare livslängd för den belagda kontakten än vad som kan vara önskvärt, särskilt i sådana kontakter som bryts och sluts ofta, eller utsätts för konstant glidning. Det finns alltså ett behov av att hitta nya ytbeläggningsmaterial som både ger en god elektrisk ledningsförmåga i en kontakt, samt är slitstarka och ger en låg friktion.

Ytbeläggningarna har syntetiserats med sk katodförstoffsning (ofta kallat sputtring, efter engelskans ord "sputtering"). Denna metod innebär att ett ursprungsmaterial atomiseras (förstoffsas) med hjälp av Ar-joner i ett plasma. Under inverkan av ett elektriskt fält accelereras Ar-jonerna mot ursprungsmaterialet, och vid kollision slås atomer ut ur ursprungsmaterialet. Den komponent man vill belägga (kallat substrat) placeras sedan så att det träffas av de utslagna atomerna, se figur 9.1, som bildar ett nytt material på ytan av substratet. Ursprungsmaterialet kan vara ett grundämne, eller en förening. I detta arbete har grundämnena använts och upp till tre separata sk källor med olika ursprungsmaterial har använts samtidigt. Detta har möjliggjort syntes av föreningar och kompositerna innehållande tre olika grundämnena i valfria proportioner. Denna process utförs i en lågtryckskammare (processen utförs i ca 1/250 000 av atmosfärstryck) och används både i industriell skala och för akademisk forskning.



Figur 9.1 Principskiss av ytbelägningsprocessen (katodförstoffsning) med en Ti- och en C-källa. Till höger visas ett foto taget under syntes av ytbeläggningar. Här syns en Ti- och Ni-källa, samt delar av en C-källa.

För att kunna bestämma de tillverkade materialens uppbyggnad och struktur har en mängd olika tekniker använts för att belysa olika aspekter av materialets uppbyggnad. Alla använda metoder har det gemensamt att man utsätter provet för strålning (synligt ljus, elektroner, röntgenstrålning eller joner) och avläser ett svar, en respons, (som kan vara i form av ljus, elektroner, röntgenstrålning eller joner). De två mest använda teknikerna har varit fotoelektronspektroskopi som används för att observera vilka grundämnena ett material innehåller och hur de är bundna till varandra, samt röntgendiffraktion som används för att karakterisera kristallina material. De karbidbaserade nanokompositernas generella struktur, så som den observerats i detta arbete, illustreras i figur 9.2.



Figur 9.2 Fyra bilder av de studerade nanokompositbeläggningarna, tagna med tre typer av olika elektronmikroskop (STEM, TEM och SEM). Vänster och mitt visar genomlysning av materialet, ovanifrån (vänster) samt från sidan (mitt). Bild till höger visar ett brottyta av en beläggning, i två olika förstoringar. Dessa bilder är tagna mha återspridda elektroner, inte i genomlysning. De tre olika delarna av figuren är från tre olika beläggningar, men de illustrerar på ett representativt sätt den generella strukturen i de karbidbaserade nanokompositbeläggningar som studerats.

Den forskning som lett fram till denna avhandling har visat att ytbeläggningar med nanokompositer bestående av nanokristallin metallkarbid (MeC_x , $\text{Me} = \text{Ti}, \text{Nb}$ eller, V) inbäddad i amorft kol (a-C) kan ge låg resistans i en elektrisk kontakt. I avhandlingen visas även att dessa material ger en låg friktion och liten nötning, varför de blir särskilt lämpade för roterande elektriska kontakter, eller kontakter som sluts och bryts ofta. I dylika tillämpningar borde karbidbaserade nanokompositer på sikt kunna ersätta dyra och mindre tåliga beläggningar av ädelmetaller.

För nanokompositer av titankarbid och amorft kol ($\text{nc-TiC}_x/\text{a-C}$) har speciella bindingsstrukturer i gränsytan mellan de båda ingående faserna påvisats. Denna gränsytebinding kan sättas i samband med tidiagre ej helt förklarade observationer i fotoelektronspektroskopi (av dessa material) och en förändring i karbidfasens struktur. Förståelse av gränsytebindningar kan i framtiden hjälpa förståelsen om hur nanokompositernas exakta egenskaper uppstår.

Genom att legera TiC_x -baserade nanokompositer med ytterligare ett metalliskt grundämne, som har en sämre förmåga att bilda kemiska bindningar till kol (här, Ni , Pt eller Cu), har ytterligare möjligheter att styra nanokompositernas mikrostruktur utforskats. Dels ändras fördelningen mellan amorft kol och karbid vilket ger ytterligare kontrollmöjligheter över mikrostrukturen, och dels bildas en metastabil övermättad blandkarbid av både metallerna, $(\text{Ti}_{1-x}\text{Me}_x)\text{C}_y$ vars kontrollerade sönderfall kan utnyttjas. Genom

val av värmebehandling kan man från sönderfallet erhålla antingen mer kolfas, eller så kan en ytterligare fas bildas av den inlösta metallen Me bildas. Den låga friktionen i denna typ av beläggningar kommer från den amorfa kolfasen, som fungerar som smörjmedel. Därför är det extra intressant att kunna kontrollera mängden kolfas. Urskiljningar av metall skulle (beroende på vilken metall det är) kunna användas för få en katalytisk verkan, eller förändra materialets optiska egenskaper.

Vid analys med fotoelektron-spektroskopi, som är väldigt ytkänslig används ofta en rengöring med högenergetiska Ar-joner (några keV:s energi) för att ta bort det yttersta ytskiktet av materialet, som alltid är oxiderat, för att därmed blotta själva materialet för analys. Resultat i denna avhandling visar att en sådan rengöring kan introducera avsevärda defekter i analysresultaten, särskilt i de fall då metastabila faser är närvarande. Detta innebär att mätningar och analyser måste utföras med eftertanke, samt att en betydande del av tidigare publicerad forskning där man använt högenergetiska Ar-joner för att blotta det material man avser analysera oavsiktligt kommit att redovisa data som kan innehålla betydande fel.

Acta Universitatis Upsaliensis

*Digital Comprehensive Summaries of Uppsala Dissertations
from the Faculty of Science and Technology 682*

Editor: The Dean of the Faculty of Science and Technology

A doctoral dissertation from the Faculty of Science and Technology, Uppsala University, is usually a summary of a number of papers. A few copies of the complete dissertation are kept at major Swedish research libraries, while the summary alone is distributed internationally through the series Digital Comprehensive Summaries of Uppsala Dissertations from the Faculty of Science and Technology. (Prior to January, 2005, the series was published under the title "Comprehensive Summaries of Uppsala Dissertations from the Faculty of Science and Technology".)



ACTA
UNIVERSITATIS
UPSALIENSIS
UPPSALA
2009

Distribution: publications.uu.se
urn:nbn:se:uu:diva-109427